J. Fluid Mech. (2025), *vol.* 1007, A29, doi:10.1017/jfm.2025.56

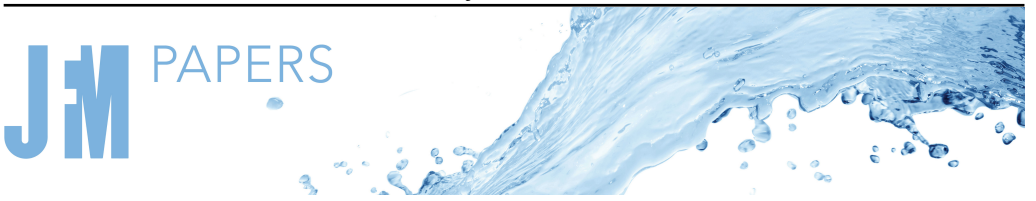

Spectral characteristics of the heat release rate in confined turbulent flames

A.D. Kumar[1], **J.C. Massey**[1,2], **A.B. Murugavel**[1], **Z.X. Chen**[3,4] and **N. Swaminathan**[1]

[1]Department of Engineering, University of Cambridge, Trumpington Street, Cambridge CB2 1PZ, UK

[2]Robinson College, University of Cambridge, Grange Road, Cambridge CB3 9AN, UK

[3]State Key Laboratory of Turbulence and Complex Systems, College of Engineering, Peking University, Beijing 100871, PR China

[4]AI for Science Institute (AISI), Beijing 100080, PR China

Corresponding author: A.D. Kumar, adk46@cam.ac.uk

(Received 5 June 2024; revised 4 October 2024; accepted 7 January 2025)

The broad-band direct combustion noise is an important problem for industrial and domestic burners. The power spectral density (PSD) of this noise is related to the local spectral density of fluctuating heat release rate (HRR) ($\psi_{\dot{q}}$), which is challenging to measure but is readily available from large eddy simulations (LES) results. The behaviour of $\psi_{\dot{q}}$ for a wide range of thermochemical and turbulence conditions is investigated. Three burners are studied, namely a dual-swirl burner, a bluff-body burner and a jet in cross-flow burner, operating at atmospheric conditions with CH_4–air and H_2–air mixtures. In contrast to the classical $f^{-5/2}$ scaling, the far-field sound pressure level and volume-integrated HRR ($\psi_{\dot{Q}}$) spectra reveal a universal f^{-5} scaling for high frequencies. This differing spectral decay rate for $\psi_{\dot{Q}}$ compared to the classical scaling is due to multi-regime combustion, related to either partial premixing or the local turbulence intensity. The dependence of $\psi_{\dot{q}}$ on the chosen spatial locations, flame configuration and its relation to velocity spectra are studied. A simple model for $\psi_{\dot{q}}$ involving the velocity spectra is found that compares well with LES results. The characteristic frequency involved in this model is related to the time scale of the coherent structures of the flow.

Key words: noise control, turbulent reacting flows, shear layers

1. Introduction

Efficient conversion of chemical energy to heat energy, commonly found in industrial and domestic applications, requires turbulent mixing of reactants, often resulting in unsteady heat release. During this energy conversion, some of the chemical energy is converted to acoustic energy as a result of the unsteadiness, which is perceived as acoustic noise. Fuel-lean and oxygen-enhanced combustion (Ehsaniderakhshan, Mazaheri & Mahmoudi 2020) are desired in practical applications such as domestic boilers, industrial furnaces and gas turbines because of their low emissions, but they are susceptible to combustion instabilities (Dowling & Hubbard 2000) and noise, which is now a critical problem (Dowling & Mahmoudi 2015). Combustion noise is emerging to be important since turbomachinery and turbulent jet noise levels have decreased significantly (Dowling & Mahmoudi 2015; Ihme 2017). Stringent noise regulations warrant the study of combustion noise from combustion systems in the above-mentioned applications.

Bushell (1971) identified an excess noise louder than the turbulent jets coming from the engine core, which has been attributed to two sources, namely, unsteady heat release rate (HRR) and density inhomogeneities (Strahle 1973, 1978). The former is known as direct noise, and the latter is referred to as indirect noise. Direct noise sources are monopoles (Dowling & Mahmoudi 2015), while jet noise sources are quadrupoles (Lighthill 1952). Indirect noise is produced by dipole sources involving entropy disturbances convected in an accelerating flow (Marble & Candel 1977). In this work, the analysis is focused on direct noise.

Theoretical and computational studies on direct noise sources and their dependence on turbulent velocity fluctuations and passive scalar spectrum were performed in the past (Klein & Kok 1999; Lieuwen *et al.* 2006). The low, high and peak frequency characteristics of the sound pressure level (SPL) were studied and compared with the HRR spectrum for a premixed Bunsen flame, revealing a remarkable correlation between the two spectra (Rajaram & Lieuwen 2009). The frequency f spectrum of SPL increases at low frequencies and decreases at high frequencies, while the peak frequency f_p scales with the convective time scale (Winkler, Wäsle & Sattelmayer 2005; Rajaram & Lieuwen 2009). In contrast to this behaviour, the volume-integrated HRR spectrum is nearly flat ($\sim f^0$) in open premixed flames (Rajaram & Lieuwen 2009), but it increases as f^3 in industrial burners (Brouzet *et al.* 2024) in the low-frequency regime, $f \leq f_p$. A fractal analysis (Clavin & Siggia 1991) reveals a high-frequency ($f > f_p$) decay rate $f^{-5/2}$ for the direct noise spectrum. Extension of such an analysis and its validity for complex practical flames is challenging and is investigated scarcely. The SPL spectra of turbulent premixed flames have an invariant shape and high-frequency characteristics irrespective of the burner nozzle shape, diameter, and incoming turbulence levels (Kotake & Takamoto 1987,1990; Tam 2015). While extensive studies have been performed on SPL spectra, HRR spectral characteristics are studied only for premixed flames (Rajaram & Lieuwen 2009; Zhang *et al.* 2019; Brouzet *et al.* 2024) using theoretical and numerical approaches.

Although most past studies focus on premixed flames, some studies on partially premixed or non-premixed flames relevant to practical combustion systems are worth mentioning. The low-frequency ($f \leq f_p$) part of the far-field SPL spectrum in non-premixed bluff-body flames operating with methane–syngas blends (Klein & Kok 1999) followed $f^{-1/2}$ behaviour compared to f^{-2} in premixed flames (Kotake & Takamoto 1987; Rajaram & Lieuwen 2009). Furthermore, the peak frequency, f_p, is lower (<100 Hz) compared to premixed flames (>100 Hz). The high-frequency ($f > f_p$) decay rates for the SPL spectrum – which is also considerably higher for non-premixed flames – range from $f^{-10/3}$ to f^{-4} (Klein & Kok 1999; Singh *et al.* 2005; Ihme, Bodony & Pitsch 2006).

The syngas flames of Klein & Kok (1999) showed a lower decay rate $f^{-10/3}$, which was captured well using a model based on the mixture fraction spectrum and the fast chemistry approach. These flames with even small amounts of methane showed a higher decay rate of f^{-4} and the reasons were attributed to finite-rate chemistry effects which is excluded in the fast chemistry approach. The partial premixing increases the SPL across the entire frequency range with the most significant increase occurring for $f > f_p$ (Singh *et al.* 2005). However, the reasons for the different high-frequency ($f > f_p$) SPL decay rates between premixed and non-premixed flames and their relation to HRR and velocity spectra remain unexplored. Therefore, the effect of mixture inhomogeneities on the HRR spectrum remains to be investigated in practical combustion systems.

While a considerable amount of work has gone into combustion noise modelling of open flames, confined flames remain relatively unexplored. The classical scaling (Clavin & Siggia 1991) $f^{-5/2}$ for the SPL is shown to hold for closed flames only when the inlet and outlet are weakly reflecting acoustic waves (Merk *et al.* 2018). Unlike open flames, confined flames have a two-way coupling between flame and acoustics. In open flames, the acoustic influence on the flame is negligible except when the flame drives the resonance of an upstream cavity (Durox *et al.* 2009). The two-way coupling is often ignored in the estimation of confined flame noise spectrum using low-order modelling (Liu *et al.* 2014; Ullrich *et al.* 2018), which leads to a reasonable agreement in the broad-band spectrum, but the narrow-band peaks are missed, if they are present. These narrow-band peaks of the acoustic spectra are captured well by considering the two-way coupling, particularly but not exclusively in the presence of intrinsic thermoacoustic instabilities (Silva *et al.* 2017; Merk *et al.* 2019). Although the two-way coupling effects on SPL have been studied using the flame transfer function (FTF) (Silva *et al.* 2017; Merk *et al.* 2019), its effect on the HRR spectrum has not been investigated directly for low frequencies. At high frequencies, the two-way coupling is known to cause broadening of the narrow-band peaks due to scattering of incident acoustic waves by the flame (Lieuwen 2001; Lieuwen *et al.* 2002).

Large eddy simulations (LES) offer high-fidelity combustion noise estimates by capturing the two-way coupling and complex flame-flow interactions, but their heavy computational cost makes a parametric sweep required for combustor design challenging. The computational overhead is larger if the far-field SPL is to be computed along with the flame–flow interactions using LES (Lyrintzis 2003). An alternative is to use a hybrid approach involving LES for near-field reacting flows and a computational aeroacoustic method for the far field (Silva *et al.* 2013). Computational costs can be further reduced by combining reduced-order modelling approaches with LES/system identification (Silva *et al.* 2017; Merk *et al.* 2019). Nonetheless, even reduced-order modelling relies on LES to provide either HRR spectra or FTF.

Several empirical models that have a substantially low computational overhead are noteworthy. Swaminathan *et al.* (2011*a*,*b*) modelled the two-point correlation of HRR, which is a central quantity for evaluating the far-field SPL. Liu & Echekki (2015) showed that two-time correlation of volume-integrated HRR models the frequency spectrum of SPL better in V-shaped open flames. Hirsch *et al.* (2007) used a modelled turbulent kinetic energy (TKE) spectrum to estimate the noise spectrum of unconfined swirling premixed flames. This required inputs (noted in Appendix A) obtained using Reynolds-averaged Navier–Stokes (RANS) simulations of reacting flows, which was shown to affect the performance of the model proposed by Hirsch *et al.* (2007) for a closed flame (Ullrich *et al.* 2018). Nonetheless, this model has not been tested rigorously for confined flames. Even in the study by Liu *et al.* (2014) where overall comparisons were reasonable, discrepancies of

up to 10 dB can be discerned between the modelled and measured spectra at frequencies away from the narrow-band peaks.

Three (two partially premixed, and one premixed) configurations that are often found in various practical applications with differing flow and flame complexities are chosen to study the HRR spectra. These configurations are (i) DLR dual swirl (Weigand *et al.* 2006; Meier, Duan & Weigand 2006), (ii) bluff body (Pan, Schmoll & Ballal 1990), and (iii) jet in cross-flow (JICF) burners (Steinberg *et al.* 2013), where the flames are stabilised aerodynamically. Most aerodynamically stabilised flames feature hydrodynamic instabilities that play a crucial role in scalar mixing and hence the flame stabilisation. For instance, swirl-stabilised flames typically feature a precessing vortex core (PVC), which is a helical hydrodynamic instability of swirling flows. Several past studies have shown its crucial role in flame stabilisation and preventing blow-off (Gupta, Lilley & Syred 1984; Froud, O'Doherty & Syred 1995; Huang & Yang 2009; Chen *et al.* 2019*a*; Massey, Langella & Swaminathan 2019*a*, 2022). Bluff-body flames feature Kelvin–Helmholtz (KH) and Bénard–von Kármán (BVK) instabilities depending on the global fuel–air mixture ratio (Emerson *et al.* 2012; Balasubramaniyan *et al.* 2021). The JICF configuration shows a rich variety of hydrodynamic features such as the counter-rotating vortex pair (CVP), upright wake vortices, shear layer vortices, near-wall vortex shedding, and horseshoe vortices (Fric & Roshko 1994; Bagheri *et al.* 2009; Karagozian 2010; Ilak *et al.* 2012). Some of these structures are the consequence of hydrodynamic instabilities such as the KH instability that results in the shear layer roll-up, the BVK instability that results in the near-wall vortex shedding in the wake of the jet that act as a soft bluff body (Bagheri *et al.* 2009; Ilak *et al.* 2012), and the elliptic instability that results in short waves on the CVP (Waleffe 1990; Fric & Roshko 1994; Karagozian 2010; Ilak *et al.* 2012). These coherent structures are crucial for flame stabilisation in reacting flows. While the roles of these coherent structures were studied recently (Brouzet *et al.* 2020) to identify sound-generation mechanisms, their influence on the spectral characteristics of the HRR is unclear, which motivates this study.

Several past studies have focused on the SPL spectra, and here our interest is on the HRR spectrum that is the direct noise source. The above discussion identifies several open questions that motivate this study. Hence the objectives here are to: (i) compare and understand the volume-integrated HRR spectrum with the local HRR spectrum and sound spectrum for partially premixed and premixed flames; (ii) understand the relationship between local HRR and velocity spectra; (iii) identify the influence of hydrodynamic instabilites on the modelling of the HRR spectrum; (iv) explore a link between the HRR and non-reacting velocity spectra. The last objective allows one to estimate the HRR spectrum, which is required for noise calculations, using the non-reacting velocity spectra, which can be measured easily.

The paper is structured as follows. Section 2 provides the mathematical background on direct noise, § 3 describes the flames analysed in this study, and § 4 outlines the methods used for data processing. The results are presented and discussed in detail in § 5. Finally, § 6 offers a brief summary of the findings.

2. Background

The inhomogeneous acoustic wave equation derived by Lighthill (1952) was generalised by Crighton *et al.* (1992) to include thermoacoustic sources. Only the unsteady HRR is the leading-order source, and all other sources can be neglected (Crighton *et al.* 1992; Swaminathan *et al.* 2011*b*). The acoustic wave equation for low Mach number flows with

the ratio of specific heat capacities γ having a weak temperature dependence is given by (Crighton *et al.* 1992; Swaminathan *et al.* 2011*b*)

$$\frac{1}{c_o^2}\frac{\partial^2 p'}{\partial t} - \frac{\partial^2 p'}{\partial x_i\,\partial x_i} = \frac{\gamma-1}{c_o^2}\frac{\partial \dot{q}'(\boldsymbol{y},t)}{\partial t}, \tag{2.1}$$

where c_o, p' and $\dot{q}'$ are the mean speed of sound in the combustion zone, pressure perturbation and HRR fluctuations per unit volume, respectively. The sound from an open flame is (Crighton *et al.* 1992)

$$p'(\boldsymbol{r},t) = \frac{\gamma-1}{4\pi r^2 c_o^2}\frac{\partial}{\partial t}\int_{V_f}\dot{q}'\left(\boldsymbol{y}, t-\frac{r}{c_o}\right)\mathrm{d}^3\boldsymbol{y}, \tag{2.2}$$

where $r = |\boldsymbol{x}-\boldsymbol{y}|$, $\boldsymbol{x}$ is the position of an observer, $\boldsymbol{y}$ is a location inside the combustion zone, t denotes time, and V_f is the volume of the combustion zone. However, in confined flames it is common to seek a Green's function solution of the form (Crighton *et al.* 1992; Liu *et al.* 2014)

$$p'(\boldsymbol{x},t) = \int_{-\infty}^{\infty}\int_{V_f} G(\boldsymbol{y},\boldsymbol{x},t-\tau)\,\frac{\partial}{\partial\tau}\left(\dot{q}'(\boldsymbol{y},\tau)\right)\mathrm{d}^3\boldsymbol{y}\,\mathrm{d}\tau, \tag{2.3}$$

where G is the Green's function representing the contribution to pressure perturbation at $(\boldsymbol{x},t)$ due to an impulse HRR per unit volume $\delta(\boldsymbol{x}-\boldsymbol{y},t-\tau)$, with the retarded time $t-\tau = |\boldsymbol{x}-\boldsymbol{y}|/c_o$. The Green's function formulation captures the pressure response of the geometry to an unsteady heat release input, but it does not recover feedback of the acoustics onto the flame. Therefore, only broad-band spectrum of pressure will be recovered in this formulation, and not narrow-band peaks arising from thermoacoustic instability. The PSD of pressure fluctuations, which is a measurable quantity in experiments, is obtained from the Fourier transform of the two-point $(\boldsymbol{y}_a,\boldsymbol{y}_b)$ correlation of pressure and its complex conjugate, resulting in (Crighton *et al.* 1992)

$$\hat{\wp}(\boldsymbol{x},f) = f^2\int_{V_f}\int_{V_f}\overline{\hat{G}(\boldsymbol{y}_a,\boldsymbol{x},f)\,\hat{G}^*(\boldsymbol{y}_b,\boldsymbol{x},f)}\cdot\psi_q(\boldsymbol{y}_a,\boldsymbol{y}_b,f)\,\mathrm{d}^3\boldsymbol{y}_a\,\mathrm{d}^3\boldsymbol{y}_b, \tag{2.4}$$

where $\psi_{\dot{q}}$ is the PSD of $\dot{q}'$ given by

$$\psi_{\dot{q}}(\boldsymbol{y}_a,\boldsymbol{y}_b,f) = \frac{1}{2\pi}\int_{-\infty}^{\infty}\underbrace{\left[\lim_{T\to\infty}\frac{1}{T}\int_0^T \dot{q}'(\boldsymbol{y}_a,t)\,\dot{q}'(\boldsymbol{y}_b,t-\tau)\,\mathrm{d}t\right]}_{R(\boldsymbol{y}_a,\boldsymbol{y}_b,\tau)=\overline{\dot{q}'(\boldsymbol{y}_a,t)\,\dot{q}'(\boldsymbol{y}_b,t-\tau)}}\mathrm{e}^{-2\pi f\tau}\,\mathrm{d}\tau. \tag{2.5}$$

Here, the overbar represents the time averaging, $*$ denotes the complex conjugate, T is a long time duration over which the samples are collected, and $R(\boldsymbol{y}_a,\boldsymbol{y}_b,\tau)$ is the space–time correlation. The Green's function does not vary much over the combustor volume (Liu *et al.* 2014), and the quantity $\psi_{\dot{q}}$ is likely to be zero beyond the volume over which $\dot{q}'$ is correlated (Swaminathan *et al.* 2011*a*). Thus integrating over the flame brush V_f is equivalent to integrating over the correlation volume V_{cor} (Wäsle 2007). The PSD of pressure fluctuations can therefore be simplified to

$$\hat{\wp}(\boldsymbol{x},f) \approx f^2\int_{V_f}|\hat{G}(\boldsymbol{y},\boldsymbol{x},f)|^2\cdot\psi_{\dot{q}}(\boldsymbol{y},f)\,V_{cor}\,\mathrm{d}^3\boldsymbol{y}, \tag{2.6}$$

and G is typically obtained numerically as has been done by Liu *et al.* (2014); however, this is not the focus of this study. The focus here is on modelling the PSD of the HRR, $\psi_{\dot{q}}$.

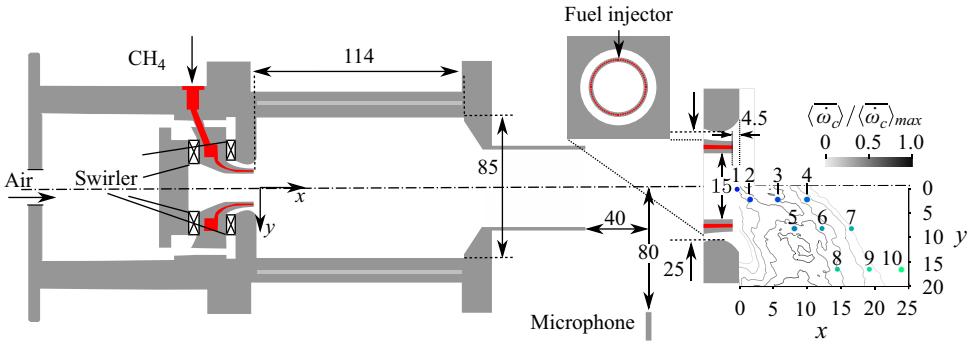

Figure 1. Schematic of the dual-swirl gas turbine model combustor (Meier *et al.* 2006; Weigand *et al.* 2006). Time series data for all quantities are extracted from the ten probe locations shown. The contour lines denote the time-averaged reaction rate of progress variable $\overline{\dot{\omega}_c}$ normalised by its maximum value. All dimensions are in mm.

Since the integral of the PSD of a quantity $\varphi(\boldsymbol{y}, t)$, $\int_0^\infty \psi_\varphi(f;\, \boldsymbol{y})\, \mathrm{d}f$, is proportional to its variance, ψ_φ is normalised as

$$\psi_\varphi^+(f;\, \boldsymbol{y}) = \frac{\psi_\varphi\,(f;\, \boldsymbol{y})}{\int_0^\infty \psi_\varphi(f;\, \boldsymbol{y})\, \mathrm{d}f}, \tag{2.7}$$

which is studied in later sections using data obtained for the three flame configurations that are described next.

3. Description of cases

3.1. *DLR dual-swirl gas turbine model combustor*

Figure 1 shows the gas turbine model combustor developed by the German Aerospace Center (DLR, Stuttgart) (Meier *et al.* 2006; Weigand *et al.* 2006). Dry air enters the plenum at room temperature, then flows through two separate swirlers. The two swirling streams enter the combustion chamber through a central nozzle of diameter 15 mm, and an annular nozzle with inner diameter 17 mm and outer diameter of 25 mm . Non-swirling methane enters the combustion chamber through a ring of 72 square channels, each with area 0.25 mm^2 . The combustion chamber has cross-section of size 85×85 mm^2 and length 114 mm . Six flames listed as DLR-A to DLR-F20 in table 1, at different heat loads and air flow rates, are simulated using LES in past studies (Chen *et al.* 2019*a*,*b*; Massey *et al.* 2019*a*,2022; Chen & Swaminathan 2020), and HRR data from those investigations are used for analysis in this work. The details of the computational and numerical schemes are discussed by Chen *et al.* (2019*a*,*b*), Chen & Swaminathan (2020) and Massey, Chen & Swaminathan (2019*a*, 2022).

3.2. *Confined bluff-body burner*

The second case considered is a bluff-body stabilised premixed flame listed as BBF in table 1. The schematic of this burner is shown in figure 2. A methane–air mixture at equivalence ratio $\phi_g = 0.59$ and inlet temperature $T_u = 294$ K enters a combustion chamber with cross-sectional area 79×79 mm^2 and length 284 mm. The cylindrical bluff body has stem diameter 12.7 mm, base diameter $D = 44.45$ mm, and apex angle $\theta = 45°$.

Case	ϕ_g	Fuel	$\dot{m}_a$ (g s^{-1})	$\dot{m}_f$ (g s^{-1})	P_{th} (kW)
DLR-A	0.65	CH_4	18.25	0.697	34.9
DLR-B (unstable)	0.75	CH_4	4.68	0.205	10.3
DLR-C	0.55	CH_4	4.68	0.15	7.6
DLR-A25NF	0.45	CH_4	5.85	0.15	7.6
DLR-A25	0.45	CH_4	5.85	0.15	7.6
DLR-F20	0.45	CH_4	4.68	0.12	6.1
BBF	0.59	CH_4	–	–	136
JICF	0.01	$H_2 + N_2$	62.12	0.18	3.0

Table 1. Reacting flow conditions for all cases.

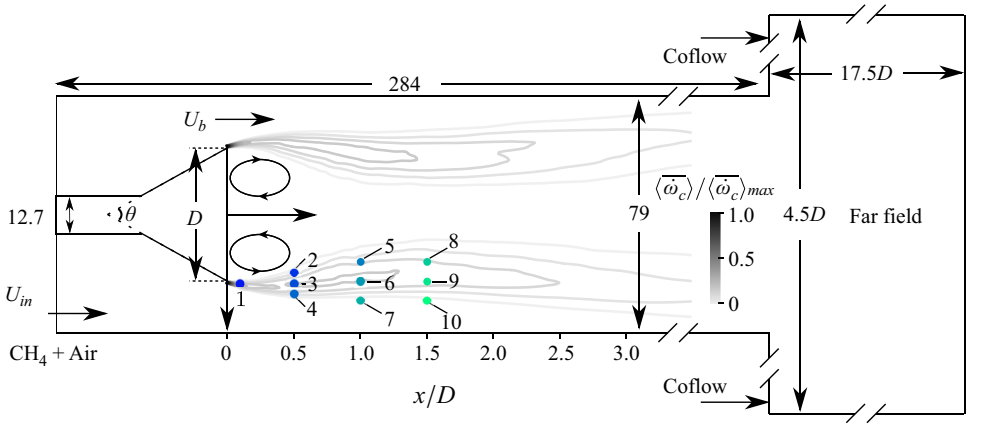

Figure 2. Schematic of the bluff-body burner (Pan *et al.* 1990; Nandula 2003). Time series data for all quantities are extracted from the ten probe locations indicated. The contour lines denote the time-averaged reaction rate of progress variable $\overline{\omega_c}$ normalised by its maximum value. All dimensions are in mm.

The bulk-mean velocity of the mixture into the combustion chamber is $U_b = 15\ \mathrm{m\,s^{-1}}$. The incoming turbulence intensity is 22 % (Langella, Swaminathan & Pitz 2016; Massey *et al.* 2019*b*, 2023). Top-hat velocity profiles with $U_{in} = 11.5\ \mathrm{m\,s^{-1}}$ are prescribed in the LES (Langella *et al.* 2016; Massey *et al.* 2019*b*, 2023), which gives $U_b = 15\ \mathrm{m\,s^{-1}}$. The midplane section of the computational domain used by Langella *et al.* (2016) and Massey *et al.* (2019*b*, 2023) is shown in figure 2, and details of the computational set-up and numerical schemes are discussed by Massey, Tanaka & Swaminathan (2023). The far-field domain was included in the LES to specify clear boundary conditions at the computational domain outlet since the flame is longer than the combustor length. The coflow condition mimics the entrainment of room air into the hot exhaust from the combustor. The conditions for one flame condition considered here are listed in table 1.

3.3. *The JICF*

The third configuration considered is the JICF depicted in figure 3, which was simulated using LES by Murugavel *et al.* (2024) and investigated experimentally by Steinberg *et al.* (2013). This flame is also listed in table 1. Preheated air at 750 K flows through a rectangular duct of size $40 \times 60\ \mathrm{mm^2}$, and fuel at 423 K is injected normally into the air stream through a nozzle of diameter $d = 2$ mm. This nozzle is flush-mounted centrally

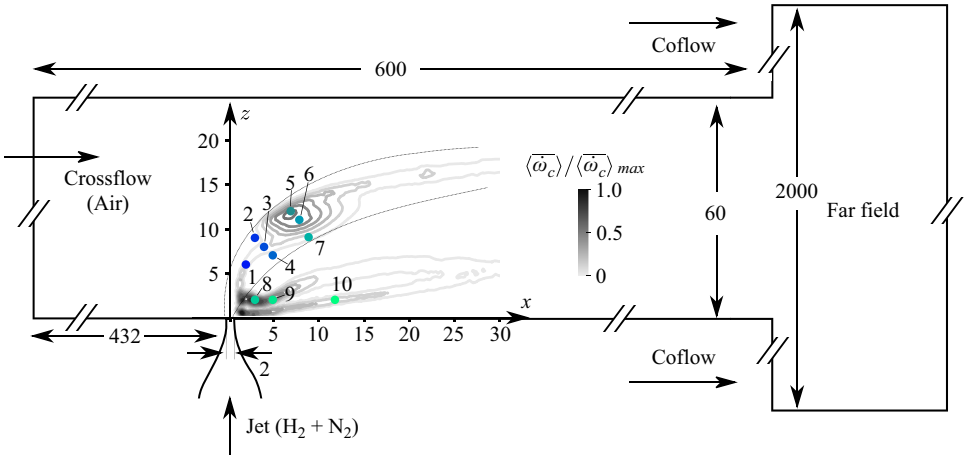

Figure 3. Schematic of the JICF burner (Steinberg *et al.* 2013). Time series data for all quantities are extracted from the ten probe locations indicated. The contour lines denote the time-averaged reaction rate of progress variable $\overline{\dot{\omega}_c}$ normalised by its maximum value. All dimensions are in mm.

on the lower wall of the duct at a distance 432 mm from the inlet, as shown in figure 3. The prescribed air mass flow rate gives bulk-mean velocity 55 m s^{-1}. The fuel stream has a mixture of 70 % H_2 and 30 % N_2 by volume. The LES results of Murugavel *et al.* (2024) are analysed to investigate the spectral characteristics of the HRR in this flame as a representative case for the JICF configuration.

To summarise, the conditions of the eight flames considered for this study are listed in table 1. Six cases in the DLR dual-swirl burner are listed, of which three cases (DLR-A25, DLR-A25NF and DLR-F20) are close to lean blow-off (Massey *et al.* 2022). For the sake of brevity, these three cases are discussed only in § 5.1 in the context of volume-integrated HRR spectra. All of these cases, except the bluff-body flame (BBF), are partially premixed flames. The fuel in all cases is CH_4 except in the JICF, where the fuel is a mixture of H_2 and inert N_2. These cases are well suited to achieve the objectives of this study since they have a wide range of flame and flow conditions along with a variety of flow features that affect the HRR and hence its PSD.

4. Data processing

4.1. *The PSD*

The LES of these eight flames were performed and validated in previous studies (Chen *et al.* 2019*a*; Massey *et al.* 2023; Murugavel *et al.* 2024). Time series of Favre filtered velocity $\widetilde{\boldsymbol{u}}$, filtered HRR $\overline{\dot{q}}$ and reaction rate of progress variable $\overline{\dot{\omega}_c}$ are extracted at ten (representative) probe points shown in figures 1–3. The variable c denoting the progress of chemical conversion of fuel to products is defined based on mass fractions Y of CO, CO_2 and H_2O as $c = \mathcal{C}/\mathcal{C}_{eq}$, with $\mathcal{C} = Y_{H_2O}$ for the JICF, and $\mathcal{C} = Y_{CO} + Y_{CO_2}$ for all other cases. The subscript 'eq' refers to the equilibrium value. The symbols $\widetilde{\square}$ and $\overline{\square}$ denoting the filtering operation will be dropped for velocity and HRR in the rest of the paper, for ease of notation.

The data sampling details are presented in table 2, where δt is the time interval of sampling, $\mathcal{T}$ is the total length of the signal in physical time, and $f_{N_s} = 1/(2\delta t)$ is the Nyquist frequency. Sampling rates for cases DLR-A25NF, DLR-A25 and DLR-F20 are

	Data sampling			Convective scaling		
Case	δt (μs)	$\mathcal{T}$ (s)	f_{N_s} (kHz)	U_b (m s^{-1})	L (m)	$f_p = U_b/L$ (Hz)
DLR-A	50	0.05485	10	19.4	0.038	510
DLR-B	120	0.09900	4.16	–	–	–
DLR-C	75	0.30000	6.66	4.0	0.028	143
BBF	50	0.20000	10	15	0.2	75
JICF	1	0.01318	500	55	0.016	3438

Table 2. Details of data sampling for all cases, and convective scaling for f_p.

identical to that of case DLR-C. The convective scaling listed in this table is discussed in § 5.1. Since case DLR-B is thermoacoustically unstable, f_p for this case does not follow the convective scaling and hence is not listed in the table. The frequency f_p corresponds to the thermoacoustic oscillation frequency as discussed in § 5.1.

The volume-integrated HRR is given by $\dot{Q}(t) = \int_{V_C} \dot{q}(\boldsymbol{y}, t)\, \mathrm{d}^3\boldsymbol{y}$, where $\dot{q}$ is the filtered HRR per unit volume. The PSD of $\dot{q}'(\boldsymbol{y}, t) = \dot{q}(\boldsymbol{y}, t) - \langle\dot{q}\rangle(\boldsymbol{y})$ or $\dot{Q}'(t) = \dot{Q}(t) - \langle\dot{Q}\rangle$ can be obtained using the Fourier transform of the respective auto-time correlation function, similar to (2.5). The PSDs of all the quantities discussed in later sections are obtained using the pspectrum function in MATLAB R2021a with frequency resolution 600 Hz for the JICF, and 80 Hz. Choosing these frequency resolutions yields smooth variations of the PSD with f.

4.2. *Overview of dynamic mode decomposition*

The PSDs will have some frequencies with significant spectral content as shown in later sections. The dynamic mode decomposition (DMD) will help to extract structures of these modes and their spatial variations unambiguously. Moreover, since one of the objectives is to analyse the influence of hydrodynamic instabilities on the local HRR spectra, the DMD of velocity field will help to identify the coherent structures associated with these instabilities, their spatial behaviour, and the associated time scales. The DMD analysis involves spatio-temporal decomposition of the field using Koopman analysis (Koopman 1931; Schmid 2010, 2022). The details and recipe for the DMD analysis can be found in Schmid (2010, 2022). Briefly, consider a general discrete nonlinear system

$$\boldsymbol{x}_{i+1} = \boldsymbol{F}(\boldsymbol{x}_i), \tag{4.1}$$

where $\boldsymbol{F}$ is matrix representation of the nonlinear governing equations that advance the dynamics of state $\boldsymbol{x}_i$ over a small time interval onto $\boldsymbol{x}_{i+1}$. Koopman analysis transforms such a finite-dimensional nonlinear system into an infinite-dimensional linear system that conveniently enables the decomposition of the spatio-temporal features of the system using properties of linear operators. Essentially, such an analysis involves a linear Koopman operator (Koopman 1931) $\boldsymbol{K}$ that advances the dynamics of the observables into their future states as follows:

$$\Theta(\boldsymbol{x}_{i+1}) = \boldsymbol{K}\, \Theta(\boldsymbol{x}_i), \tag{4.2}$$

where Θ is a function embedding the state $\boldsymbol{x}$ such that (4.2) is satisfied. The DMD is applied in this study to extract the spectral properties (eigenvalues and eigenvectors) of such a Koopman operator (Schmid 2010, 2022). It is assumed throughout this study that $\Theta(\boldsymbol{x}) = \boldsymbol{x}$, a commonly used notion in fluid dynamics. This assumption is deemed

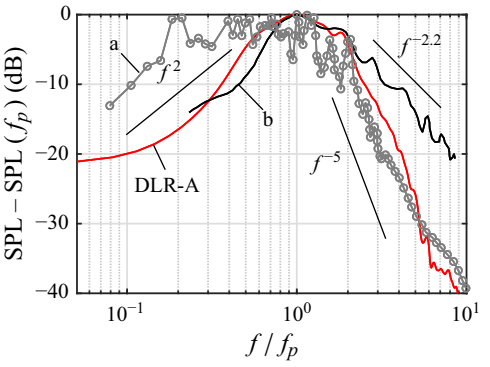

Figure 4. Measured SPL for DLR-A, a non-premixed jet (marked as a) (Singh, Frankel & Gore 2004) flames and a piloted premixed Bunsen (marked as b) (Rajaram & Lieuwen 2009). Here, $\mathrm{SPL}(f) = 10\log(\hat{\wp}/p_{ref}^2)$, where $p_{ref} = 20\,\mu\mathrm{Pa}$.

sufficient for the purpose of extracting coherent structures in frequency space. The modal amplitudes b, indicating the strengths of the DMD modes, are obtained based on past work (Jovanović *et al.* 2014) with weights assigned according to the growth rate of each mode (Tu *et al.* 2014).

5. Results and discussion

The SPL and volume-integrated HRR PSDs are presented and discussed in this section, followed by a detailed discussion on the characteristics of the local HRR PSD. The similarities and differences between the local and volume-integrated HRR PSDs are discussed, and the underlying reasons are inferred from the LES results. Finally, a suitable model for the local HRR PSD is proposed and validated in the last subsection.

5.1. *The SPL and volume-integrated HRR spectra*

The SPL and the volume-integrated HRR spectra were shown to be correlated for open turbulent premixed (Rajaram & Lieuwen 2009) and non-premixed (Ihme *et al.* 2006) flames. However, in confined flames, the PSD of pressure is not directly related to volume-integrated HRR only as demonstrated by (2.6). The Green's function is the pressure generated in response to an impulse of rate of heat addition. Since the flame is generally compact and the mixing is fast, the acoustic impedance of the combustor is nearly constant in the axial direction. Additionally, since the combustor geometry is typically axially uniform, the Green's function does not vary much in the axial direction. At low frequencies, the higher contributions to Green's function from the lower mode numbers are compensated by the lower contributions from the higher mode numbers. The trend reverses at higher frequencies (Liu *et al.* 2014) and therefore yields a Green's function spectrum whose frequency variation is typically within one decade. Therefore, the typical Green's function spectrum $|\hat{G}(\boldsymbol{y}, \boldsymbol{x}, f)|^2$ does not vary much with f or axial distance, as shown for an industrial combustor by Liu *et al.* (2014). This suggests that the SPL and the volume-integrated HRR spectrum may indeed be correlated even in confined flames. Hence it is of fundamental interest to assess the effect of partial premixing and confinement on this correlation. Before analysing the HRR signal, the measured SPL for DLR-A is compared with results from past works of unconfined turbulent premixed (Rajaram & Lieuwen 2009) and non-premixed (Singh *et al.* 2004) jet flames in figure 4. In order to make meaningful

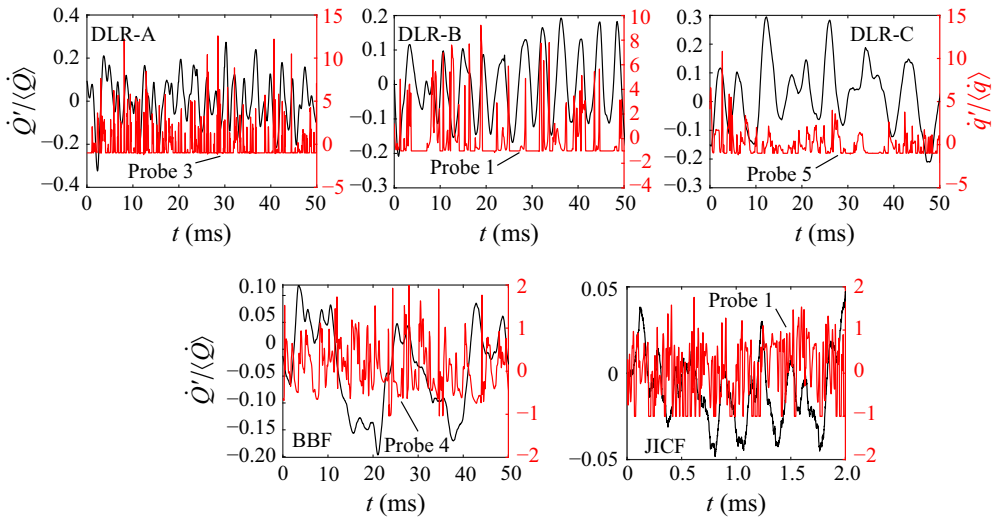

Figure 5. Time series $\dot{Q}'$ and $\dot{q}'$ normalised by their respective time averages for cases DLR-A, DLR-B, DLR-C, BBF and JICF. The typical local HRR data are shown for arbitrary probe locations indicated.

comparisons, the spectra are shifted appropriately to match the peak SPL in both cases. The spectra show an approximate power-law dependence of f^2 at low frequencies for all cases. This is consistent with a past study (Rajaram & Lieuwen 2009) which showed $\hat{\wp}(\boldsymbol{x}, f) \sim f^2 \psi^+_{\dot{Q}}$. It will be shown next that the volume-integrated HRR spectrum $\psi_{\dot{Q}}$ is flat in this frequency range. The high-frequency part ($f > f_p$) falls off as f^{-5} for DLR-A and the turbulent non-premixed jet (Singh *et al.* 2004) flames as compared to $f^{-2.2}$ for the premixed piloted flame (Rajaram & Lieuwen 2009). While the low-frequency spectra are approximately comparable for all cases, the high-frequency spectra show a substantial difference between the cases. The reasons for this difference can be understood by studying the HRR spectrum.

First, the temporal behaviour of $\dot{Q}'$ and $\dot{q}'$ is studied before analysing their frequency spectra. These results are shown in figure 5, normalised using the respective time averages. Note that $\langle\dot{Q}\rangle = P_{th}$, as given in table 1. The local HRR, $\dot{q}(\boldsymbol{y}, t)$, is driven by a small-scale phenomenon, hence it is highly intermittent, resulting in $|\dot{q}'| > \langle\dot{q}\rangle$ as observed in many past studies (Swaminathan *et al.* 2011*b*; Liu & Echekki 2015). The local HRR vanishes ($\dot{q} = 0$) for the partially premixed flames whenever the local mixture fraction value is not within the flammability limits, hence the negative fluctuations of $\dot{q}$ are limited to $\dot{q}' = -\langle\dot{q}\rangle$. Since $\dot{Q}(t)$ is a volume-integrated quantity that is mostly driven by large-scale flow structures, it varies smoothly with t.

Figure 6(*a*) shows the variation of $\psi^+_{\dot{Q}}$ (see (2.7)) with f for the eight cases listed in table 1. The normalised PSDs for all the cases, except for JICF, fall in the same frequency range. In the JICF case, variations are across a broader and higher frequency range ($10^3 < f \leq 10^5$) due to the higher-frequency hydrodynamics present in this flow. Additionally, this may be attributed to the faster burning rates of the H_2/N_2 fuel mixture, as discussed in the next subsection. Figure 6(*b*) shows the variation of $\psi^+_{\dot{Q}}$ with f/f_p, where f_p is given by a convective scaling (Winkler *et al.* 2005; Rajaram & Lieuwen 2009) listed in table 2. Such a scaling denotes the time scale for large-scale fluctuations convected over characteristic length scale L by the bulk-mean velocity U_b. The bulk-mean velocity in the partially premixed cases is obtained as $U_b = \dot{m}/\rho_a A_{in}$, where

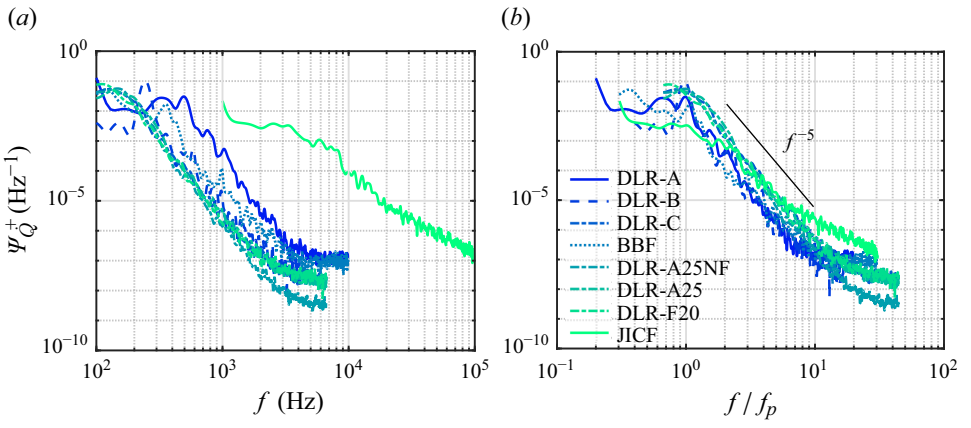

Figure 6. The variation of $\psi^+_{\dot{Q}}$ with (*a*) f and (*b*) f/f_p.

$\dot{m} = \dot{m}_a(1 + (\dot{m}_f/\dot{m}_a)_{st}\phi_g)$, ρ_a is the air density, and A_{in} is the cross-sectional area of the combustor inlet. The quantity $(\dot{m}_f/\dot{m}_a)_{st}$ is the stoichiometric fuel–air mass ratio, and typically $(\dot{m}_f/\dot{m}_a)_{st}\phi_g \ll 1$. The characteristic length is taken to be the flame length, which is defined as the distance between the flame root and the streamwise location of the maximum time-averaged reaction rate of progress variable $\langle\overline{\dot{\omega}_c}\rangle$, for the DLR flames. For the BBF case, it is approximated as the length of the combustor since the flame brush extends outside the combustor. The flame length for the JICF case is defined as the curvilinear distance between the jet exit and the point along the jet centreline where the maximum $\langle\overline{\dot{\omega}_c}\rangle$ occurs. The DLR-B flame is thermoacoustically unstable, therefore the threshold frequency beyond which $\psi^+_{\dot{Q}}$ decays is given by the frequency of thermoacoustic oscillation $f_p = f_T \approx 250$ Hz. The variation of $\psi^+_{\dot{Q}}$ with f for $f < f_p$ is negligible, as has been observed in past studies (Rajaram & Lieuwen 2009), and the collapse in the normalised frequency space is reasonable. The convective scaling (U_b/L) for f_p listed in table 2 agrees well with the results seen in figure 6(*a*).

At high frequencies ($f > f_p$), the normalised PSD for most cases decays at an identical rate of approximately f^{-5}, which is quite remarkable. The JICF case decays at a slightly lower rate for $f > f_p$, which is the result of the high-frequency dynamics discussed later in § 5.2. This high-frequency decay rate f^{-5} is considerably higher than the previously measured (Rajaram & Lieuwen 2009) ($f^{-2.2}$) or theoretically deduced ($f^{-2.5}$) (Clavin & Siggia 1991) rates. The high-frequency spectral decay rate for $\dot{Q}'$ marked in figure 6(*b*) is identical to the SPL fall-off rate shown in figure 4. This strongly suggests that the Green's function frequency spectrum (see (2.6)) has little variation with f, as observed by Liu *et al.* (2014). Therefore, the strong correlation between $\psi^+_{\dot{Q}}$ and SPL observed for premixed unconfined turbulent flames (Rajaram & Lieuwen 2009) holds for confined– both premixed and partially premixed– flames also. It is remarkable that these flames with different complexities show almost the same spectral decay f^{-5}. It is instructive to analyse the spectra of $\psi_{\dot{q}}$ to gather more insights. The local spectrum is particularly important for cases when there is significant spatial and frequency variation of the Green's function. For example, cases with effusion cooling, non-compact flames, multi-stage combustion and the presence of azimuthal modes (Liu *et al.* 2014) result in significant spatial and frequency variation of the Green's function. In such cases, the sound pressure spectrum cannot be directly related to $\psi_{\dot{Q}}$.

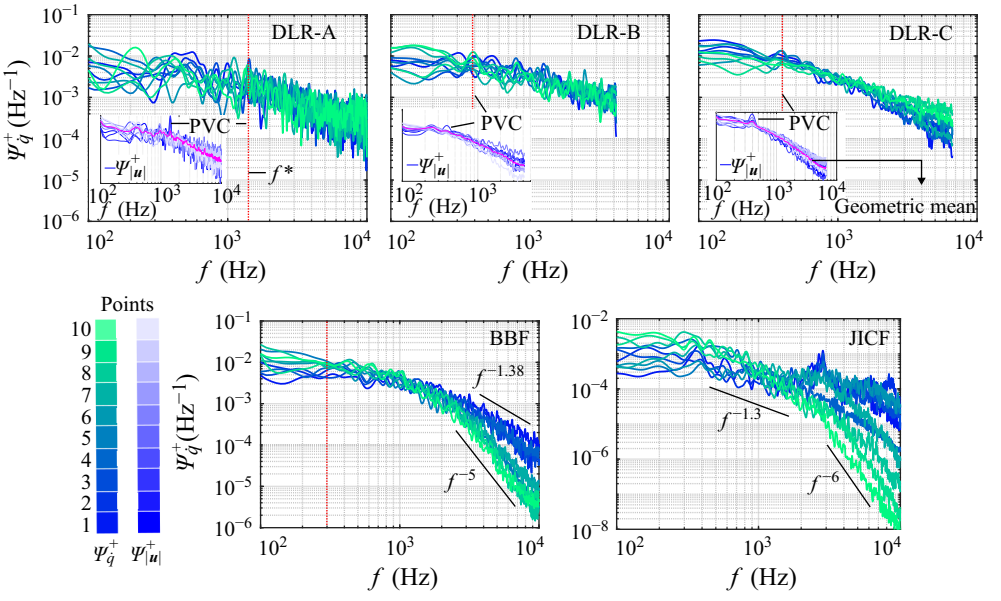

Figure 7. The variation of $\psi_{\dot{q}}^+$ with f at ten probe locations for the five cases. The insets in the DLR cases show the normalised PSD of velocity magnitude, $\psi_{|\boldsymbol{u}|}^+$, for the same probe locations. The magenta line shows the geometric mean of $\psi_{|\boldsymbol{u}|}^+$ at the ten probe locations. The vertical red dotted line marks the characteristic frequency f^*.

5.2. *Local HRR spectra*

The local instantaneous HRR $\dot{q}(\boldsymbol{y}, t)$ data are collected for ten probe locations shown in figures 1–3. The normalised PSD $\psi_{\dot{q}}^+(f)$ at these ten locations for the five cases listed in table 2 are shown in figure 7 along with the velocity spectra for the DLR flames. The PSDs can be segregated into two regimes, namely, a low-frequency regime $f < f^*$ and a high-frequency regime $f > f^*$, where f^* is the characteristic frequency marked using vertical red dotted lines. The frequency beyond which the PSD starts to fall off is defined to be the characteristic frequency f^* here. The PSD $\psi_{\dot{q}}^+(f)$ is more or less constant, with a small amount of scatter across the spatial points for all the cases when $f \leq f^*$. A peak near the PVC frequency is evident in the inset showing $\psi_{|\boldsymbol{u}|}^+(f)$. This is marked as PVC in figure 7, and it is seen only for probe locations close to this flow structure. The PVC is a distinct coherent structure modulating the flame surface in these cases (Chen *et al.* 2019*a*; Massey *et al.* 2019*a*), and is responsible for the high spectral content for frequencies close to the PVC frequency. Therefore, the characteristic frequency f^* for the local HRR spectra is equal to the PVC frequency in these cases. The spectra decay for $f > f^*$, and there is some small spatial variation of $\psi_{\dot{q}}^+$. The PSD of the BBF case in figure 7 shows a slightly different spectral behaviour, although the overall qualitative trend across the frequency space is similar to the DLR flames. The low-frequency behaviour has only a small variation similar to DLR flames, as seen in the figure. The spectral roll-off rate for all the locations is similar for $f > f^*$ up to approximately 3 kHz. The spectral decay is faster for higher f, and is also moving downstream, as indicated by lighter colour curves. The decay exponent varies from 1.38 for the most upstream locations to 5 for the most downstream locations, as shown in figure 7. The normalised PSD of HRR for the JICF flame has several similarities and differences compared to the other cases. It is similar

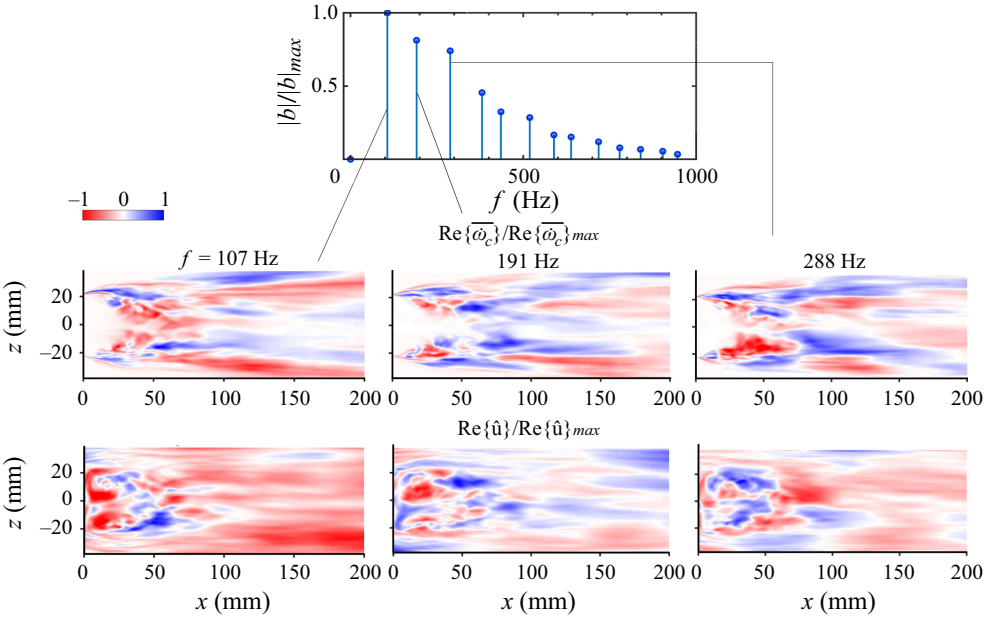

Figure 8. DMD mode amplitude of $\overline{\dot{\omega}_c}$ and $|\boldsymbol{u}|$ for the BBF case, and the spatial distribution of three dominant modes.

to the other spectra since it qualitatively captures the same trend. However, there are at least two key differences: (i) there is a significant variation of the normalised PSD across different locations at high frequencies with a discernible narrow-band peak; and (ii) the entire spectral content is shifted to a higher (by one order of magnitude) frequency regime. The decay rates show a substantial spatial variation similar to the BBF case beyond $f \approx$ 27 kHz. However, unlike the DLR cases, identifying a physically meaningful threshold frequency is challenging and is sought out next using DMD analyses.

Peaks are observed in neither $\psi_{\dot{q}}^{+}$ nor $\psi_{|\boldsymbol{u}|}^{+}$ (not shown) for the BBF case, suggesting that no globally unstable hydrodynamic mode is excited. It is therefore more challenging to identify a physically motivated characteristic frequency f^* for this case. To proceed further, a simultaneous DMD of the reaction rate and velocity magnitude is performed. The results are shown in the mid x–z plane to recognise dominant coherent structures and their modal energy, which could assist in the identification of a suitable f^*. A total of 200 DMD modes m, where each mode corresponds to a particular frequency, are used for this analysis, and this number of modes is deemed sufficient since at least 80 % of the energy content is captured. Figure 8 shows the DMD mode amplitudes $|b|$ normalised by their peak values, and the mode shapes for the three most dominant modes. The mode shapes of the reaction rate of progress variable and velocity magnitude ($\mathrm{Re}\{\widehat{\dot{\omega}_c}\}/\mathrm{Re}\{\widehat{\dot{\omega}_c}\}_{max}$ and $\mathrm{Re}\{\hat{\boldsymbol{u}}\}/\mathrm{Re}\{\hat{\boldsymbol{u}}\}_{max}$), shown in figure 8 are essentially the real parts of the eigenvectors of the Koopman operator $\boldsymbol{K}$ (see (4.2)) obtained using DMD. The velocity modes do not reveal distinct coherent structures; however, the HRRs show a greater degree of coherence as seen from the large areas of either blue or red colour in figure 8, especially in the shear layers where the flame is stabilised. The three most dominant modes recognised using DMD show an antisymmetric (sinuous) pattern about $z = 0$ mm for the HRR, which is most evident at $f = 288$ Hz. The lack of substantial coherence and a subsequent globally

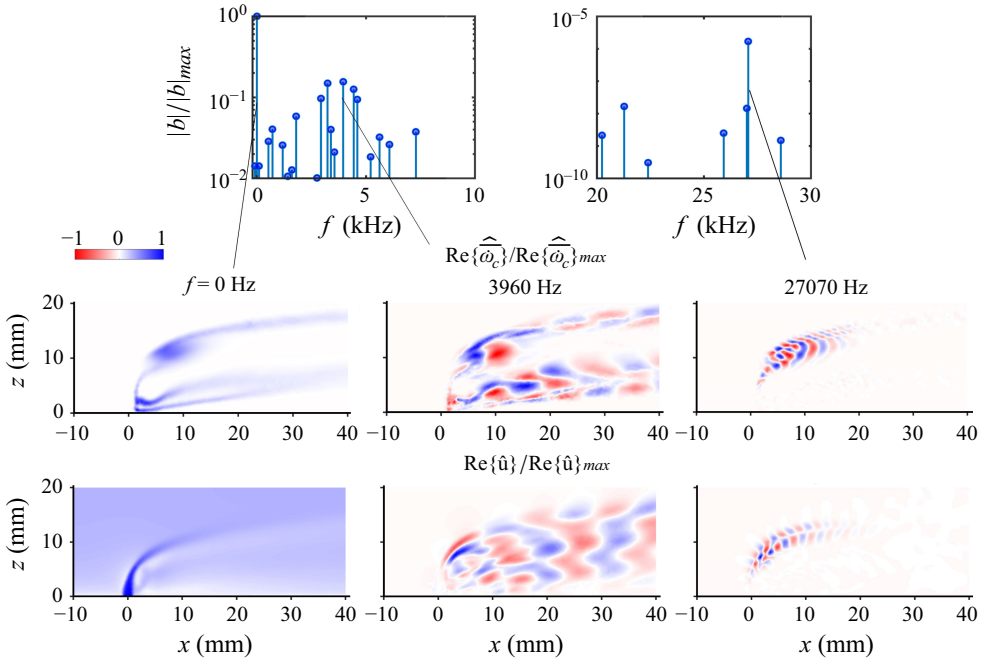

Figure 9. The DMD mode amplitude of $\overline{\dot{\omega}_c}$ and $|\boldsymbol{u}|$ for the JICF flame, and the spatial distribution of three modes.

unstable mode is most likely due to the high turbulence intensity (22 %) in this case. Since the modal amplitudes are high in the frequency range $100 < f < 300$ Hz before substantial decay occurs, as seen in the top row of figure 8, the spectral characteristic frequency can be conveniently identified in this range. The precise value of the characteristic frequency in this range is not critical for the analysis since it will be shown to have negligible impact on modelling aspects discussed later in § 5.3.

Figure 9 shows the DMD results for the reacting JICF obtained using 350 modes, which sufficiently capture over 80 % of the energy content. The DMD reveals that the zero-frequency mean flow is the most dominant mode that features two branches for the real part of the reaction rate. The second most dominant mode, at $f = 3960$ Hz, resembles an elliptic short-wavelength (about 5 times the jet exit diameter) instability of the CVP in the jet region similar to past studies (Laporte & Corjon 2000; Ilak *et al.* 2012). This instability is most evident in the region $20 < x < 40$ mm and $10 < z < 20$ mm where an antisymmetric mode structure in $\widehat{\dot{\omega}_c}$ is clearly visible, and this is a characteristic of the short-wavelength elliptic instability of the vortex pairs. This instability results in short waves convecting along the jet trajectory. Furthermore, this mode shows the upright wake vortices being distorted by the background flow in the wake region ($10 < x < 40$ mm and $0 < z < 10$ mm) as is evident in both the velocity and the reaction rate mode structures. These structures also convect along the cross-flow similarly to the short waves on the CVP. This second mode showing the elliptic instability and wake vortices results in a wide region of coherence, hence the corresponding frequency is a reasonable choice for the characteristic frequency in this case. An additional DMD mode can be recognised at $f = 27\,070$ Hz as shown in figure 9, which is close to the narrow-band peak observed

in figure 7 for the JICF case. Note that the spatial window used for the DMD is much wider than the spatial extent of this mode. Therefore, the mode amplitudes that optimise the faithful modal reconstruction of the entire flow field are heavily weighted against modes that have a short spatial extent in comparison to the entire DMD window. As a result, extremely low amplitudes (note the scale on the y-axis) are seen for this mode, which is active only in a small region close to the jet shear layer. This mode structure closely resembles the typical shear layer roll-up due to KH instability, as seen clearly from the antisymmetric mode structure for velocity magnitude. The reaction rate mode structure shows a complex structure for $0 < x < 10$ mm, possibly from the distortions of the flame surface caused by the shear layer vortices. However, at $x > 10$ mm the mode structure changes to alternating cusp-like structures before quickly diminishing in strength. These coherent structures significantly increase the spectral content of $\psi_{\dot{q}}^{+}$ and explain the narrow-band peak seen in figure 7 for the JICF case.

The spatially varying decay rates seen for cases BBF and JICF in figure 7 may be understood by analysing the chemical time scale defined as $\tau_c = \overline{\rho}/\overline{\dot{\omega}_c}$. The increasing decay rates for $\psi_{\dot{q}}^{+}$ with downstream locations in the BBF case suggest that the local chemical time scale variation identified by Langella *et al.* (2016) may play a role. Figure 10(*a*) shows the probability density function (PDF) of τ_c^{-1} for the three different regions shown in the right-hand column, depicting the spatial variation of time-averaged reaction rate $\overline{\dot{\omega}_c}$ in the mid x–z or x–y plane. It is clear that τ_c increases, and smaller time scales become less probable, with downstream distance, as shown in figure 10(*a*). Therefore, a multi-regime combustion occurs in this case (Langella *et al.* 2016). Fast time scales (high frequencies) have lower spectral content since large reaction rates do not occur at downstream locations. This explains the influence of the spatially varying chemical time scale on the subsequent high-frequency ($f > 3$ kHz) spectral decay rates seen in figure 7 for the BBF case. Similarly, zone S3 in figure 10 has the largest chemical time scale and subsequently highest spectral decay rate in figure 7 for the JICF case. In contrast, zone S1 has the lowest chemical time scale, and as a result it also has the lowest decay rate, while zone S2, which is on the leeward side of the jet exit, takes intermediate values. The PDFs of chemical time scales in the swirling flow cases are much narrower, and the distributions do not differ substantially between different spatial locations, as seen in figure 10(*c*) for the DLR-B flame. Similar behaviour is observed for other DLR flames listed in table 2. Therefore, the spectral decay rate of $\psi_{\dot{q}}^{+}$ for the swirl-stabilised flames are quite similar across different locations.

In light of the results above, it is interesting to compare the characteristics of $\psi_{\dot{q}}^{+}$ and $\psi_{\dot{Q}}^{+}$. The low-frequency spectral content in both these spectra shows a near constant trend below a characteristic frequency (f_p for $\psi_{\dot{Q}}^{+}$, and f^* for $\psi_{\dot{q}}^{+}$) for all cases. However, these characteristic frequencies differ considerably for all the cases except JICF. The characteristic frequency in the local spectra generally corresponds to a hydrodynamic instability, as discussed earlier in this subsection. The nearly flat spectral content at $f < f^*$ suggests that the local fluctuations are coherent at time scales close to those induced by the coherent motions of the hydrodynamic mode. The frequency f_p for $\psi_{\dot{Q}}^{+}$ depends on the convective scaling U_b/L_f for all the cases except DLR-B (thermoacoustically unstable flame), as discussed in the previous subsection. The characteristic frequencies for the JICF case compare well between the normalised PSDs of local and global HRR. Since f^* is dictated by the hydrodynamic modes of convective nature (short-wave elliptic instability and wake vortices) with large spatial extent, it is expected that the global PSD also would have similar characteristic frequency. In contrast, the swirl-stabilised flames are influenced

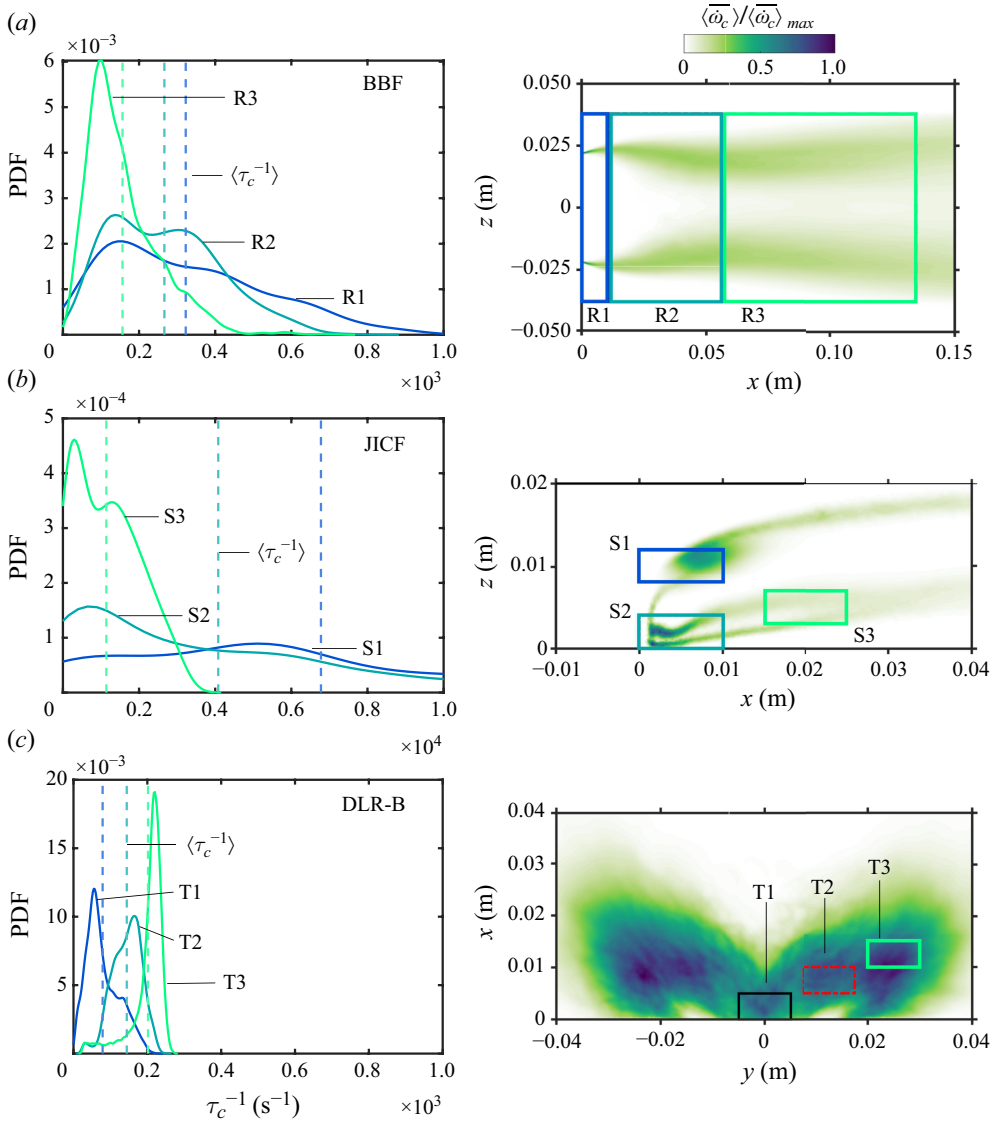

Figure 10. The PDFs of τ_c for three spatial zones marked in the right-hand column showing $\langle\dot{\omega}_c\rangle/\langle\dot{\omega}_c\rangle_{max}$. The dashed vertical lines indicate the mean τ_c^{-1} in each zone.

locally by the PVC, which is not a convective mode aligned with the bulk flow. Therefore, one can expect a significant difference between f_p and f^*, for instance, $f_p = 510$ Hz whereas $f^* = 1400$ Hz for the DLR-A flame.

The high-frequency spectral decay rates show a vast difference between the normalised PSDs of local and global HRR. The spectral decay ranges from f^{-1} to f^{-6} for $\psi^+_{\dot{q}}$, whereas the spectral decay for $\psi^+_{\dot{Q}}$ varies mostly as f^{-5}. The difference in spectral decay rates between the global and local HRR can be assessed using the framework described in Lieuwen (2012). According to this framework, the global HRR spectrum is related to the following physical factors: (i) the local HRR spectra, which depend on velocity fluctuations (Clavin & Siggia 1991) and equivalence ratio fluctuations as in

this work; (ii) spectral variation of correlation volume ($V_{corr}(f)$); and (iii) convection of fluctuations due to tangential flow along the flame (Rajaram & Lieuwen 2009; Lieuwen 2012). Therefore, the difference between the local and global HRR spectral decay rates must arise from the spectral characteristics of the correlation volume and/or the phase cancellation due to tangential convection of fluctuations along the flame front. Lieuwen (2012) shows that the global and local heat release spectra are related to each other using the correlation length scale, also known as the coherence length scale (Rajaram & Lieuwen 2009). The three-dimensional analogue of this relation is given by

$$\frac{\psi_{\dot{Q}}^{+}}{V_F^2} \approx \begin{cases} \psi_{\dot{q}}^{+}, & \mathcal{O}(V_{cor}) \sim \mathcal{O}(V_F), \\ 8\psi_{\dot{q}}^{+}\,\dfrac{V_{cor}(f)}{V_F} + \mathcal{O}\left(\dfrac{V_{cor}(f)}{V_F}\right)^2, & \mathcal{O}(V_{cor}) \ll \mathcal{O}(V_F), \end{cases} \tag{5.1}$$

where instead of correlation length, l_{cor}, correlation volume V_{cor} is used, and V_F is the flame volume. Since V_{cor} decays with increasing frequency (Rajaram & Lieuwen 2009; Lieuwen 2012), it can be seen from (5.1) that at frequencies where $\mathcal{O}(V_{cor}) \ll \mathcal{O}(V_F)$, the decay rate of $\psi_{\dot{Q}}^{+}$ will exceed that of $\psi_{\dot{q}}^{+}$. The correlation volume is proportional to the product of the correlation length scales in the three directions (Wäsle *et al.* 2005). The correlation length scale in each direction can be computed by fitting the decay of the coherence to the following equation (Rajaram & Lieuwen 2009):

$$\gamma^2\,(x, x+\Delta x, f) = \exp\left(-\frac{\Delta x}{l_{cor}\,(f)}\right)^2, \tag{5.2}$$

where Δx is the separation between an arbitrary point of interest within the flame region and the location of maximum heat release. The coherence γ^2 is given by

$$\gamma^2\,(x, x+\Delta x, f) = \frac{|\check{\psi}_{\dot{q}}\,(x, x+\Delta x, f)\,|^2}{\check{\psi}_{\dot{q}}\,(x, x, f)\;\check{\psi}_{\dot{q}}\,(x+\Delta x, x+\Delta x, f)}, \tag{5.3}$$

where $\check{\psi}_{\dot{q}}$ is the PSD of the transversely integrated HRR given by

$$\check{\psi}_{\dot{q}} = \int\int \psi_{\dot{q}}\,\mathrm{d}y\,\mathrm{d}z. \tag{5.4}$$

The correlation length scales in the other directions (y and z) are computed similarly.

The results for the spectrum of correlation volume for three representative cases are shown in figure 11(*a*). The correlation volume decays as frequency increases for all cases, with the highest decay rate for case DLR-B, which approaches f^{-3}. The comparatively faster decay of V_{cor} for the partially premixed cases is likely due to the mixture inhomogeneities. The slower decay rate of V_{cor} for the JICF case is likely due to the presence of high-frequency hydrodynamic instabilities that maintain a large level of coherence and ensure strong mixing.

Additionally, consider the cross-spectrum phase of transversely integrated HRR, $\varphi_{\dot{q}}(\Delta, f) = \arg\{\check{\psi}_{\dot{q}}(x, x+\Delta, f)\}$, which is useful to discern the contribution of phase cancellation due to convective phenomena. The phase cancellation due to convection of fluctuation along the flame front also results in the decay of global HRR spectrum proportional to f^{-2} at high frequencies. In the presence of convective phenomena, it is possible to identify a convective velocity or phase velocity v_φ defined as

$$v_\varphi = \left|\frac{\partial^2 \varphi_{\dot{q}}}{\partial f\;\partial \Delta x}\right|^{-1}. \tag{5.5}$$

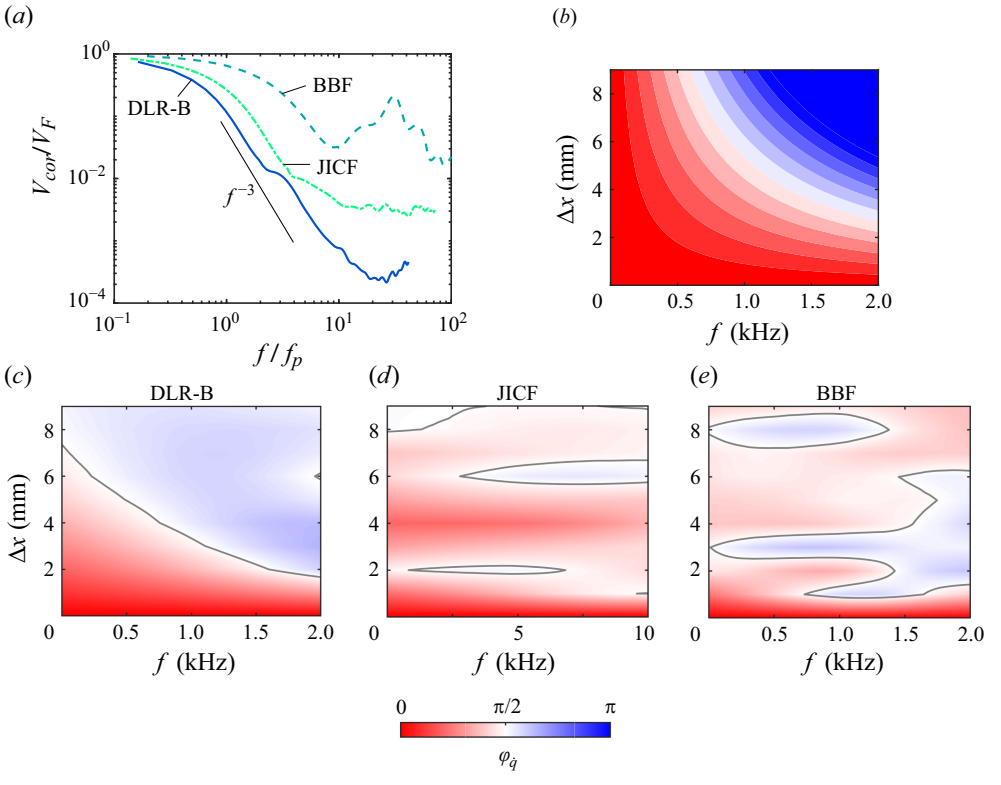

Figure 11. (*a*) The frequency spectrum of the correlation volume normalised by the flame volume V_F. (*b–e*) Contours of cross-spectrum phase $\varphi_{\dot{q}}$ of transversely integrated HRR along (y, z) for a synthetic signal and cases DLR-B, JICF and BBF. Grey contour lines denote the mark $\varphi_{\dot{q}} = \pi/2$.

Figure 11(*b*) shows the representative cross-spectrum for an arbitrary synthetic signal with $\varphi = (\pi/10)\, f\, \Delta$ and a constant phase velocity $v_\varphi = 10/\pi$ m s^{-1}. The contours of the cross-spectrum phase for the three cases are shown in figures 11(*c–e*). It can be seen that the contours of $\varphi_{\dot{q}}$ for case DLR-B are qualitatively similar to figure 11(*b*), suggesting the presence of convective phenomena. However, there are at least two quantitative differences in the phase characteristics of the synthetic signal and case DLR-B. The phase velocities in the case DLR-B are not exactly constant throughout the $(f, \Delta x)$ space (not shown), and unlike in the synthetic signal, $f = 0$ is not an asymptote in the case DLR-B, possibly due to the inadequate low-frequency resolution of the LES. The other cases, namely JICF and BBF, do not show similar smooth hyperbolic contours and a smooth transition from in-phase oscillations ($\varphi_{\dot{q}} < \pi/2$) to out-of-phase oscillations ($\varphi_{\dot{q}} > \pi/2$) as f and Δx increase. Therefore, there are no discernible convective phenomena in these cases.

The high-frequency spectral decay rate $\psi^+_{\dot{Q}}$ for the partially premixed DLR case and premixed BBF case are identical despite the difference in decay rates of V_{cor}. This is because the decay rate $\psi^+_{\dot{q}}$ increases with increasing downstream distance, as discussed previously in figure 7, and this compensates for the higher level of coherence in the BBF case. This feature of the BBF is further exemplified by showing the normalised PSD of area-integrated $\overline{\dot{\omega}_c}$ in three different regions, as shown in figure 12(*a*). The higher level of coherence in the JICF flame at high frequencies results in a slightly lower spectral decay rate for $f/f_p > 1$, as seen in figure 6(*b*). The lower spectral decay at high frequencies can

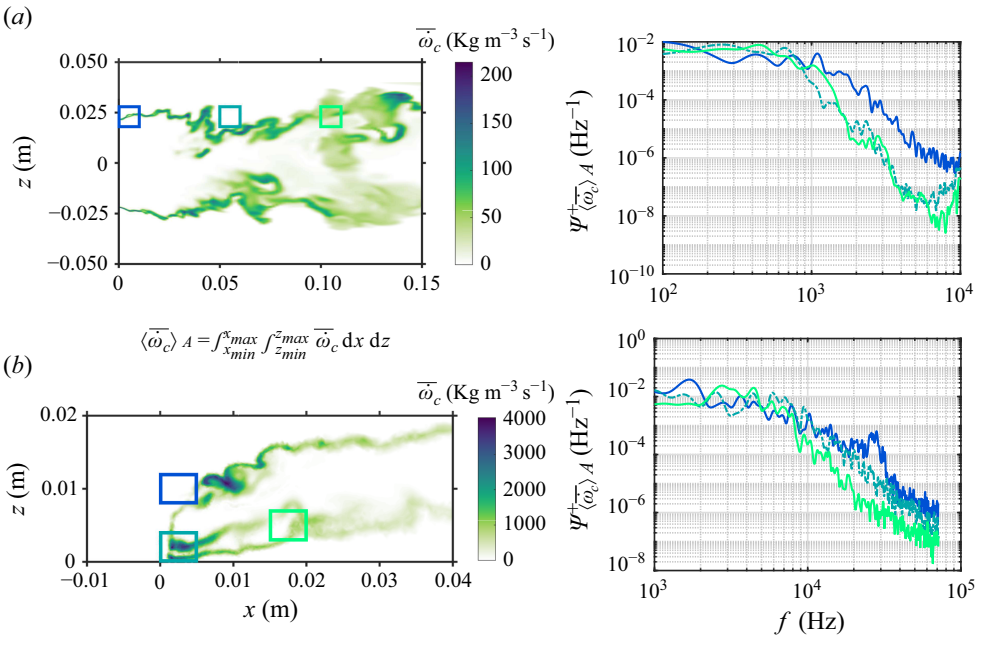

Figure 12. Instantaneous $\overline{\dot{\omega}_c}$ in the mid x–z plane, and the PSD of the area-integrated $\overline{\dot{\omega}_c}$ in the three regions marked for (*a*) BBF and (*b*) JICF flames.

also be due to finite rate chemistry effects of pure H_2. A past study showed that the syngas mixtures had lower decay rates in comparison with syngas and methane blends due to finite-rate chemistry effects (Klein & Kok 1999). Therefore, presence of methane should result in larger τ_c values. This is consistent with the results in figure 10, where τ_c for the JICF case, which operates on H_2 fuel, is lower compared to the BBF or DLR-B cases operating with pure methane fuel. Therefore, the presence of hydrogen and its inherent high burning rate may also contribute to the lower spectral decay rate of $\psi^+_{\dot{Q}}$ for the JICF flame. The complementary roles played by chemical kinetics and hydrodynamics on $\psi^+_{\dot{Q}}$ is further exemplified by computing the area-integrated $\overline{\dot{\omega}_c}$ for three different regions shown in figure 12(*b*). The area-integrated reaction rate spectra show different spectral decay rates for the three locations, as seen in figure 12(*b*). The region enclosed by the blue box is close to the shear layer roll-up, which occurs at approximately 27 kHz, hence the spectral decay rate is elevated in this region. To further understand the competing effects of chemical kinetics and hydrodynamics on the spectral decay rates requires studying the JICF flame with different fuels, such as methane, which is a future study.

In summary, the combination of decaying V_{cor} spectrum and phase cancellation due to convection of perturbations along the flame front is responsible for the vast disparity in decay rates between the local and global HRR spectra for the DLR cases. While there is no convective phase cancellation in the JICF and BBF cases, the spatially decaying local HRR spectra along with the decay of the V_{cor} spectra result in a similar disparity of decay rates between the local and global HRR spectra for these cases. It is also noted that the decay of the V_{cor} spectra in the different cases is dependent on the presence of mixture inhomogeneities, the presence of hydrodynamic instabilities, and finite-rate chemistry effects.

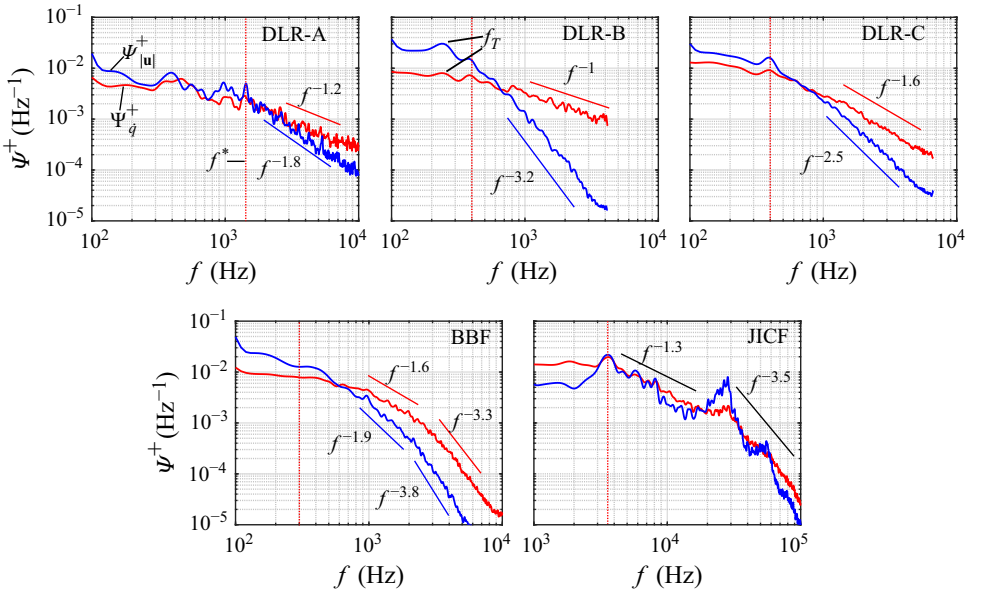

Figure 13. Geometric mean normalised spectra of local HRR and velocity magnitude for the respective cases. The vertical red dotted line marks the characteristic frequency f^*.

5.3. *Modelling aspects*

For modelling purposes, it is interesting to compare the normalised PSDs of HRR and velocity magnitude. For the sake of simplicity, it is important to consider a meaningful mean PSD that closely approximates the spatial variation of $\psi^+_{\dot{q}}$ shown in figure 7. The DLR cases show negligible spatial variation and are hence insensitive to the way the mean PSD is obtained. However, the BBF and JICF flames showing a large spatial variation demand an appropriate way to calculate a representative mean PSD. An arithmetic mean may not be suitable for this purpose since it would heavily favour locations with large spectral content. Therefore, a geometric mean is used to obtain a representative PSD for the BBF and JICF flames.

The geometric mean of normalised $\psi^+_{\dot{q}}$ and $\psi^+_{|\boldsymbol{u}|}$ is shown in figure 13 for all the cases. This geometric mean is denoted using Ψ with appropriate subscripts. The decay rate for $\Psi^+_{\dot{q}}$ ranges from 1 to 3.5 for all cases, whereas the range is from 1.8 to 3.8 for $\Psi^+_{|\boldsymbol{u}|}$. The PSDs for the DLR-A flame remain nearly constant up to $f^* \approx 1400$ Hz, which is identical to the PVC frequency. At $f > f^*$, the spectra decays at the rates 1.2 and 1.8 for the HRR and velocity PSDs, respectively. In contrast to the DLR-A flame, the thermoacoustically unstable DLR-B flame has two characteristic frequencies – thermoacoustic frequency f_T, and PVC frequency f^*. The characteristic frequency for $\Psi^+_{|\boldsymbol{u}|}$ is identical to the thermoacoustic frequency f_T. It is surprising to note that the characteristic frequency for $\psi^+_{\dot{Q}}(f_p)$ is equal to $f_T = 250$ Hz (see figure 6*a*), whereas it is equal to the PVC frequency $f^* = 400$ Hz for $\Psi^+_{\dot{q}}$. These results can be explained using a past LES study focusing on the flame leading edge movement in this case (Chen *et al.* 2019*a*). It was shown that the azimuthal movement of the flame leading point is strongly correlated with the PVC frequency, suggesting that the local HRR would be strongly influenced by the PVC, resulting in a small peak at f^*, as seen in figure 13 for the DLR-B flame. Even though the DLR-B flame has thermoacoustic oscillations, the local HRR – unlike the

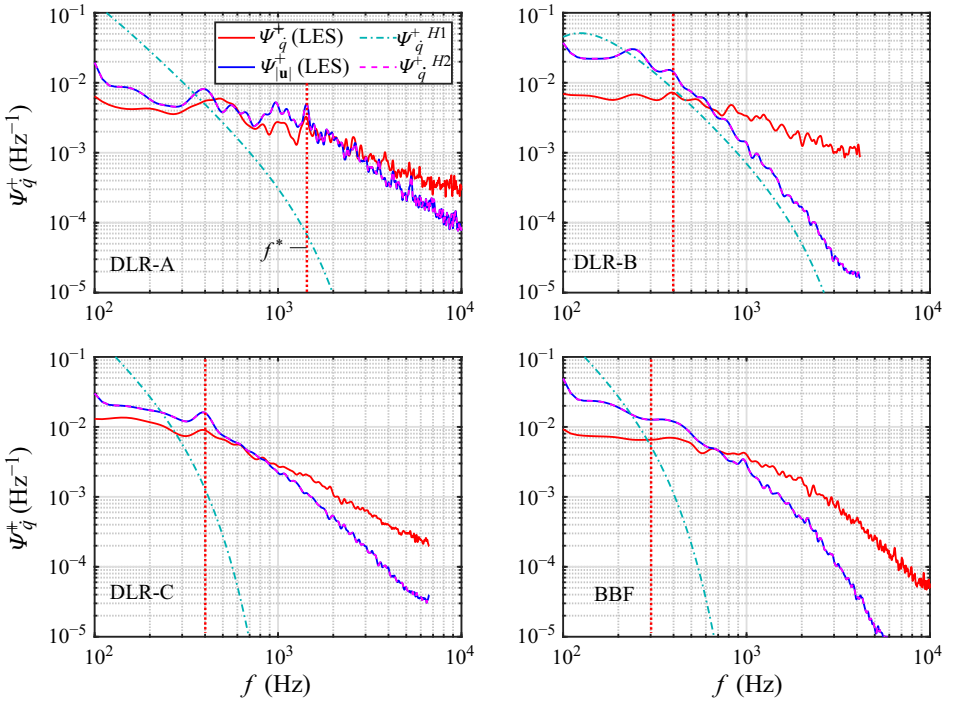

Figure 14. Comparison of model spectrum (Hirsch *et al.* 2007) for $\Psi_{\dot{q}}^{+}$ with LES results for the DLR flames and BBF case. The vertical red dotted line denotes f^*.

global HRR– is influenced both by local activity such as the local mixing, PVC, etc., and by the thermoacoustic oscillation. However, the velocity fields are substantially modulated only by the thermoacoustic oscillation, hence the high-frequency spectral decay rates for HRR and velocity magnitude PSDs are more disparate in the DLR-B flame compared to other cases. Furthermore, the cumulative spectral content for $f > f_T$ has to compensate for the accumulation of spectral content at $f = f_T$ due to the thermoacoustic oscillation resulting in a higher spectral decay rate for $\Psi_{|\boldsymbol{u}|}$.

The DLR-C flame shows a trend similar to that of the DLR-A flame in figure 13, with slightly larger decay rates 1.6 and 2.5 for the HRR and velocity magnitude PSDs, respectively. The characteristic frequency f^* for the DLR-C flame is equal to the PVC frequency 400 Hz . In the BBF case, the spectral decay rates for $\Psi_{\dot{q}}^{+}$ and $\Psi_{|\boldsymbol{u}|}^{+}$ in the approximate range $1000 \lessapprox f \lessapprox 3000$ Hz are 1.6 and 1.9, respectively, as seen in figure 13. At approximately 3 kHz, the spectral decay rate increases to 3.3 for HRR and 3.8 for $\Psi_{|\boldsymbol{u}|}^{+}$. The increase in the decay rate is due to the increase in τ_c as discussed previously. The JICF PSD shows a characteristic frequency $f^* \approx 3500$ Hz that corresponds to the combined wake-vortex and elliptic instability mode of the CVP. The spectral decay rate is identical for the HRR and velocity magnitude PSDs, and is equal to 1.3 in the approximate range $3.5 \lessapprox f \lessapprox 27$ kHz, and 3.5 for $f \gtrapprox 27$ kHz. The shear layer vortex roll-up results in a narrow-band peak at approximately 27 kHz as discussed previously in figure 12.

A key observation from figure 13 is that the spectral decay rates of HRR and velocity magnitude are not the same, and it is consistently lower for the former for all cases except JICF. This observation highlights the limitations of existing models (Hirsch *et al.* 2007)

Parameter	Values			
	DLR-A	DLR-B	DLR-C	BBF
$\dot{q}_o$ (GW m^{-3})	0.1	0.5	0.07	1.15
$Y_{F,0}$	0.0368	0.042	0.0311	0.0332
a_0 (μm^2 s^{-1})	14.8	14.8	14.8	14.8
H_u (MJ kg^{-1} s^{-1})	50	50	50	50
ρ_0 (kg m^{-3})	1.18	1.18	1.18	1.18
u' (m s^{-1})	12.36	2.78	3.59	3.63
t_I (ms)	0.26	1.3	0.76	0.38
Λ (mm)	3.3	3.6	2.7	1.4
$\widetilde{\epsilon}$ (m^2 s^{-3})	5.8×10^5	6.03×10^3	1.69×10^4	3.43×10^4
$\widetilde{k}$ (m^2 s^{-2})	229.34	11.59	19.38	19.8
s_L (m s^{-1})	0.12	0.2	0.08	0.09
Da_t	0.024	0.32	0.03	0.02
η_{c^2} (μm)	8.64	27.7	20.9	17.5
L_G (μm)	8.64	1.33	0.03	0.02
L_C (μm)	0.003	27.7	20.9	17.5

Table 3. Description and values of parameters in Hirsch's model (Hirsch *et al.* 2007) for cases DLR-A, B, C and BBF.

for HRR spectra deduced using the velocity spectra. Furthermore, the velocity spectra do not exactly follow the Kolmogorov $-5/3$ law ($-5/2$ in frequency space; Clavin & Siggia 1991) for such complex cases, as is often assumed in existing models.

Before proceeding further it is necessary to gauge the performance of existing models, such as that proposed by Hirsch *et al.* (2007), which is described in Appendix A. The quantity $\Psi_{\dot{q}}^{+}$ estimated using this model for the DLR flames and BBF case are shown in figure 14 alongside the velocity magnitude PSD. Two variations of this model are shown, where $\Psi_{\dot{q}}^{+H1}$ is the original model (Hirsch *et al.* 2007) and $\Psi_{\dot{q}}^{+H2}$ uses the LES velocity spectrum instead of the one-dimensional model spectrum by Tennekes & Lumley (1972). The modelled $\Psi_{\dot{q}}^{+H1}$ shows severe inaccuracies in the low, characteristic and high frequency characteristics for all cases. The modified model ($\Psi_{\dot{q}}^{+H2}$) is identical to the velocity spectrum due to normalisation. While the modified spectrum performs better than $\Psi_{\dot{q}}^{+H1}$ in capturing the qualitative trends, it does not account for the disparity in the spectral decay rates between $\Psi_{|\boldsymbol{u}|}^{+}$ and $\Psi_{\dot{q}}^{+}$ discussed previously in this subsection. Another conceptual limitation of this model is the assumption that the scalar dissipation rate of reactive progress variable can be modelled using the linear relaxation model used for passive scalars (Pierce & Moin 1998). Several past studies have shown that this assumption is problematic in turbulent premixed flames where the flame dilatation has a significant contribution to the scalar dissipation rate that the linear relaxation model fails to capture (Swaminathan & Bray 2005; Dunstan *et al.* 2013). While the model is strictly applicable only to premixed flames, an approximation for laminar flame speed is obtained based on the global equivalence ratio (ϕ_g) for the partially premixed swirl stabilised flames. Such a model is also inapplicable in cases where the global equivalence ratio is well below the lower flammability limit, as in the case of the JICF flame. The values of the various parameters involved are listed in table 3 for all cases shown in figure 14.

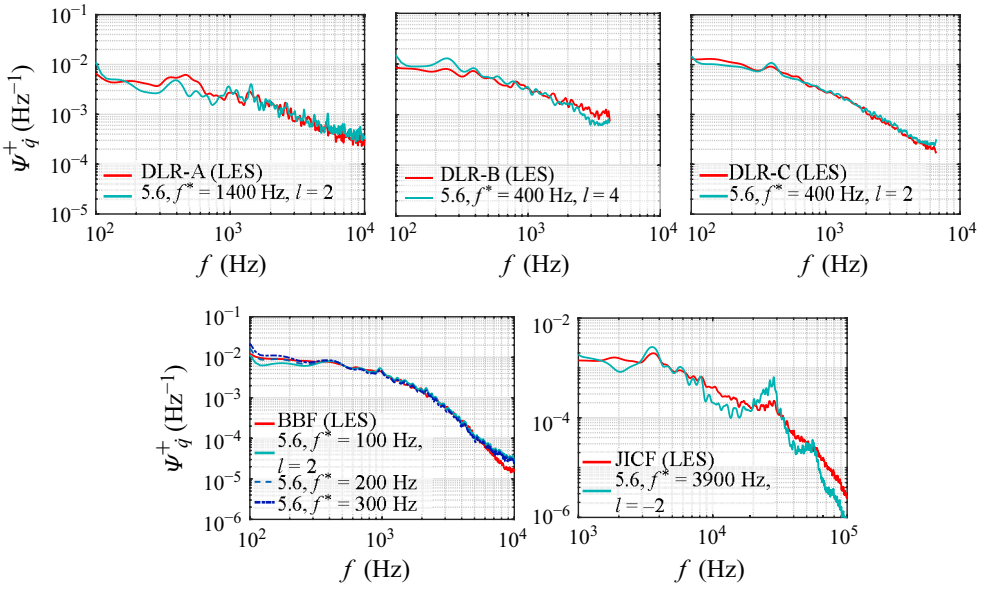

Figure 15. Comparison of computed (see figure 13) and modelled (see (5.6)) $\Psi^+_{\dot{q}}$ for the respective cases.

To account for the difference in spectral decay rates between velocity magnitude and HRR PSD, the following model is proposed in this work:

$$\Psi^+_{\dot{q}} \approx \Psi^+_{|\boldsymbol{u}|}\left(1+\left(\frac{f}{f^*}\right)^{l}\right)^{1/2}, \tag{5.6}$$

where f^* and l are the characteristic frequency for $\Psi^+_{\dot{q}}$ and scaling exponent, respectively. This model is considerably simpler compared to that in Hirsch *et al.* (2007), with only two parameters, and depends on $\Psi^+_{|\boldsymbol{u}|}$ obtained from reacting flow LES.

The comparison of this modelled and computed $\Psi^+_{\dot{q}}$ is shown in figure 15. The model compares well with the LES spectrum for all the cases. Since no clear unstable hydrodynamic mode was identifiable in the BBF case, the characteristic frequency is chosen in the range $100 < f < 300$ Hz as discussed previously, and weak sensitivity of the PSD is seen for the choice of f^*. This sensitivity is seen only for $f \leq 200$ Hz for the BBF case. The scaling exponent is $l = 2$ except in the DLR-B and JICF flames. The higher scaling exponent for the DLR-B flame is because of its thermoacoustic instability, which resulted in a larger disparity in the decay rates between $\Psi^+_{\dot{q}}$ and $\Psi^+_{|\boldsymbol{u}|}$ as seen in figure 13. The scaling exponent is much lower and negative for the JICF flame. This is because of the high-frequency dynamics associated with hydrodynamic instabilities, which results in nearly identical decay rates for $\Psi^+_{\dot{q}}$ and $\Psi^+_{|\boldsymbol{u}|}$ as seen in figure 13. The HRR is not an easy quantity to measure in experiments, but $\psi^+_{|\boldsymbol{u}|}$ may be measured relatively easily. Hence (5.6) can conveniently model $\Psi^+_{\dot{q}}$. This model has several advantages over that suggested by Hirsch *et al.* (2007). First, this model uses reacting velocity spectra instead of Kolmogorov's model spectra for homogeneous isotropic turbulence, which is most often inapplicable in practical flows. Second, the model captures well the considerable difference in the spectral decay rates seen for all the cases. Third, this model is physically motivated using the characteristic frequencies associated with hydrodynamic modes for

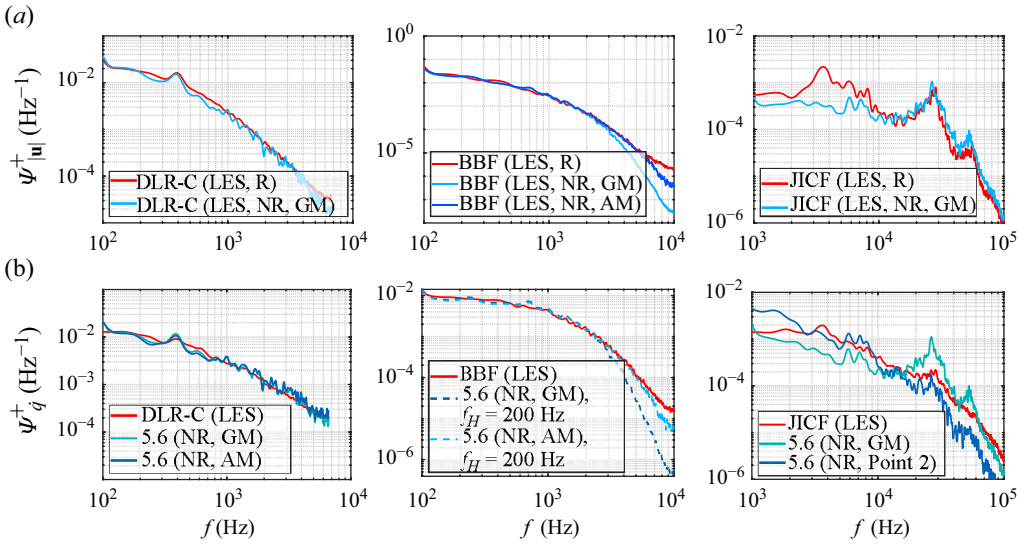

Figure 16. (*a*) Comparison of mean reacting (R) and non-reacting (NR) $\Psi^+_{|\boldsymbol{u}|}$, and (*b*) comparison of LES results and model (5.6), using normalised NR velocity magnitude PSD for DLR-C, BBF and JICF. Here, AM means arithmetic mean, and GM means geometric mean.

aerodynamically stabilised flames. Finally, this model is fairly robust across the cases and uses only one parameter, the exponent l. A limitation of this model, however, is its reliance on computationally expensive reacting flow simulations to obtain the velocity magnitude PSD $\Psi^+_{|\boldsymbol{u}|}$. It is therefore interesting to investigate whether the non-reacting flow is sufficient to model the HRR spectra. Figure 16(*a*) compares the reacting and non-reacting $\Psi^+_{|\boldsymbol{u}|}$ for three representative cases (DLR-C, BBF and JICF). The results for DLR-A are expected to be qualitatively similar to the DLR-C flame. This model is inappropriate for case DLR-B since the non-reacting flow is inherently missing the two-way coupling between flame and acoustics necessary for this unstable case. The reacting flow-based model works well, as shown in figure 15, since this coupling is present in the reacting flow velocity spectra. The non-reacting $\Psi^+_{|\boldsymbol{u}|}$ is obtained as the geometric mean of $\psi^+_{|\boldsymbol{u}|}$ gathered for ten probe locations in the respective non-reacting cases. The peak at approximately 400 Hz in figure 16(*a*) for the DLR-C case corresponds to the PVC frequency, which is nearly identical between the reacting and non-reacting flows. In the case of BBF, the reacting and non-reacting counterparts are identical up to 3 kHz when using the geometric mean. The comparisons improve using the arithmetic mean, which tends to favour higher spectral content of the upstream locations. The discrepancy between the arithmetic and geometric means arises because the velocity spectra decay at a faster rate with downstream distance for the non-reacting case compared to the reacting case. This is possibly a result of flame dilatation increasing the spectral content in the reacting case (Bilger 2004; Kolla *et al.* 2014). The reacting and non-reacting $\Psi^+_{|\boldsymbol{u}|}$ spectra for the partially premixed cases are not affected much by this effect (Bilger 2004; Knaus & Pantano 2009). The reacting and non-reacting spectra are similar in their broad-band nature and the high-frequency range for the JICF case. The shear layer roll-up is dominant in both reacting and non-reacting conditions, resulting in the local narrow-band peak. The interaction between the flame, wake vortices and the short-wave instability of the CVP is strong enough to result in a peak at $f \approx 3500$ Hz in the reacting velocity spectra for this case. However, the absence of such an interaction in the non-reacting flow at these

time scales does not result in a prominent narrow-band peak in the local non-reacting $\Psi^+_{|\boldsymbol{u}|}$. These results suggest that the $\Psi^+_{|\boldsymbol{u}|}$ from non-reacting flow represents $\Psi^+_{\dot{q}}$ based on (5.6), although some differences may be expected.

Figure 16(*b*) compares $\Psi^+_{\dot{q}}$ obtained using (5.6) with non-reacting flow $\Psi^+_{|\boldsymbol{u}|}$ from the corresponding LES for the three cases discussed previously. The comparisons are reasonable for DLR-C, and the spectra show a negligible sensitivity to the method of obtaining the mean. The results for the other DLR flames is also expected to be similar to the DLR-C flame. Figure 16(*b*) for BBF shows that the arithmetic mean captures the HRR spectra with improved accuracy especially at very high frequencies ($f > 2$ kHz), for reasons discussed previously. The comparisons for the JICF case are reasonable with discrepancies in the low-frequency regime ($f < 10$ kHz) and at the narrow-band peak at $f \approx 27$ kHz. The discrepancy in the narrow-band peak is because of the stronger peak in the velocity spectra compared to the HRR spectra. The discrepancy in the low-frequency range is due to the differences seen in the comparisons between the normalised reacting and non-reacting velocity magnitude PSDs in figure 16(*a*) for the JICF. The comparisons are improved significantly by using the velocity spectra from a location away from the shear layer roll-up (point 2 in figure 3). The improvements are obtained because of the lower spectral content at high frequencies ($f > 20$ kHz) for this location, which lowers the discrepancy in the narrow-band peak at $f \approx 27$ kHz observed previously. To summarise, the non-reacting velocity spectra, but not the Kolmogorov spectra, are sufficient to model the HRR spectra using (5.6) since the parameters f^* and l remain approximately unchanged between the reacting and non-reacting flows as they are related to the hydrodynamics.

6. Summary and conclusions

The spectral characteristics of local and global HRR, which are relevant to the direct combustion noise, are investigated for several aerodynamically stabilised flames using LES data. Five cases at atmospheric conditions in three configurations, namely, DLR dual-swirl burner, bluff-body burner and JICF, are investigated with CH_4–air and H_2–air mixtures. This work aims to understand the spectral behaviour of HRR so that a reliable and robust model for these spectra can be developed.

The spectral characteristics of global HRR PSD for all the cases and measured far-field noise spectra for the DLR-A flame show the same spectral decay f^{-5} at high frequencies. This is substantially higher than previously observed $f^{-5/2}$ behaviour in open flames (Clavin & Siggia 1991; Rajaram & Lieuwen 2009). It is concluded that the lower spectral coherence in the local HRR due to mixture inhomogeneities in enclosed partially premixed flames is the reason for higher spectral decay rates in the global HRR spectra. The spectral decay rates are influenced significantly by the spatially varying chemical time scales within the combustion zone observed for the BBF and JICF cases. The characteristic frequencies for the global HRR PSD are equal to the inverse of a convective time scale, defined as the ratio of convective velocity and an appropriate flame length for most cases.

The spectral characteristics of local HRR are qualitatively similar to the global HRR spectra. However, the characteristic frequency is associated with a physically important hydrodynamic mode for all the cases studied, and their high-frequency spectral decay is significantly lower than the global counterpart. The dominant hydrodynamic mode in the dual-swirl cases is the PVC, which maintains a strong level of coherence at frequencies close to f_{PVC}. The hydrodynamic modes in the BBF and JICF flames are identified using DMD analysis. The characteristic frequency of the local HRR spectra in the JICF flame is equal to the frequency at which the wake vortices and the short-wave elliptic instability

arise. This frequency in the bluff body stabilised flame is associated not with any dominant global hydrodynamic mode but with a collection of a few modes in the frequency range 100–300 Hz. The spatial distribution of mode amplitudes in this frequency range shows antisymmetric patterns of the shear layer about the bluff-body centreline.

Finally, a new model is proposed that is physically motivated by coherent structures of the flow field, has fewer empirical constants, and is shown to be robust across the cases considered in this work. This model uses the reacting flow velocity spectra, and accurately estimates the HRR spectra for all cases. An alternative model that uses the non-reacting velocity spectra is also proposed, revealing satisfactory results. The model based on the non-reacting velocity incurs substantially lower computational costs than the reacting counterpart. Additionally, this model accurately captures the HRR spectra without relying on simple one-dimensional TKE model spectra (Tennekes & Lumley 1972) that may not be strictly valid for such reacting flows in complex practical systems.

Acknowledgements. A.D.K. acknowledges financial support from the Cambridge Trust. The University of Cambridge authors acknowledge support from Mitsubishi Heavy Industries, Ltd, Japan. This work used the ARCHER2 UK National Supercomputing Service (https://www.archer2.ac.uk). We would like to thank one of the anonymous reviewers for suggesting the discussion on correlation volume spectra and phase cancellation effects due to convection.

Funding. The authors are grateful to the EPSRC (grant no. EP/R029369/1) and ARCHER2 for financial and computational support as a part of their funding to the UK Consortium on Turbulent Reacting Flows (https://www.ukctrf.com).

Declaration of interests. The authors report no conflict of interest.

Data availability statement. The data will be made available upon reasonable request.

Author contributions. A.D.K. and N.S. conceptualised the work. J.C.M. simulated cases BBF and DLR-C; Z.X.C. simulated cases DLR-A and DLR-B; and A.B.M. simulated case JICF. A.D.K. performed the post-processing, data analysis and data curation. J.C.M. and A.B.M. performed additional simulations and post-processing to aid the analysis. N.S. was responsible for supervision and acquiring funding for the Cambridge authors. A.D.K. wrote the original draft, and all authors contributed to reviewing and editing the manuscript.

Appendix A

The model spectrum in the wavenumber (κ) space proposed by Hirsch *et al.* (2007) is given by

$$E_{\dot{q}}^{H1}(\kappa) = \dot{q}_o C_s C_D \,\widetilde{\epsilon}^{2/3}\,\widetilde{k}^{-1}\kappa^{-5/3} \times \exp\left[-\frac{3}{2}\left(\pi\beta\alpha^{1/2}\,(\kappa\Lambda)\right)^{-4/3} + \alpha\left(\kappa\eta_{c^2}\right)^{4/3}\right], \tag{A1a}$$

$$\dot{q}_o = 4.96\frac{\widetilde{\epsilon}}{\widetilde{k}}\left(\frac{s_L}{\sqrt{2/3}} + \left(1 + Da_t^{-2}\right)^{-0.25}\right)^2 \times \widetilde{c} \times (1-\widetilde{c})\,\rho_0 Y_{F,0} H_u, \tag{A1b}$$

$$Da_t = \frac{0.09\,\widetilde{k}\,s_L^2}{\widetilde{\epsilon}\,C_c^2\,a_0} \quad \text{and} \quad C_s = \frac{\alpha}{C_D}\left(\frac{\dfrac{s_L}{\sqrt{2/3\widetilde{k}}} + \left(1 + Da_t^{-2}\right)^{-0.25}}{\dfrac{s_L}{\sqrt{2/3\widetilde{k}} + 1}}\right)^2, \tag{A1c}$$

where $C_D = 2.0$, $\alpha = 1.5$, $\beta = 0.3$ and $C_c = 1.2$ are model constants, and the other parameters are listed in table 3. These parameters are scaled mean HRR per unit volume

$\dot{q}_o$, reactant fuel mass fraction $Y_{F,0}$, kinematic viscosity of the unburnt mixture a_0, lower heating value of the fuel H_u, reactant density ρ_0, root mean square velocity u', integral time scale t_I, integral length scale Λ, TKE $\widetilde{k}$, dissipation rate of TKE $\widetilde{\epsilon}$, laminar flame speed s_L, turbulent Damköhler number Da_t, diffusive length scale $\eta_{c^2} = \max[c_G L_G, L_C]$, model constant $c_G = 3$, Gibson length scale L_G, and Corrsin length scale, L_C. The values of model constants and other modelling details can be found in Hirsch *et al.* (2007) and Liu *et al.* (2014). The model is based on the assumption that the HRR spectrum is proportional to the reactive scalar spectrum, which is thereby proportional to the the TKE spectrum. The TKE spectrum is given by the classical model spectrum of Tennekes & Lumley (1972), whose validity for the operating conditions considered in this work has to be tested. The model one-dimensional TKE spectrum (Tennekes & Lumley 1972) may not strictly be valid in the cases considered, hence an alternative model given by

$$E_{\dot{q}}^{H2}(\kappa) = \dot{q}_o \frac{C_D C_s}{\alpha} \widetilde{k}^{-1} E_{u^2}, \tag{A2}$$

where E_{u^2} is the TKE spectrum obtained directly from the reacting flow LES, is proposed. The spectrum is transformed from the wavenumber space to the frequency space following Tennekes & Lumley (1972), which requires the conservation of the spectral content across the two spaces $\kappa E_{\dot{q}} = 2\pi f \psi_{\dot{q}}$, and assuming simple rearrangement between the Lagrangian and Eulerian frameworks. The details of the transformation to frequency space can be found in Hirsch *et al.* (2007) and Liu *et al.* (2014). The mean normalised PSDs for the two models are obtained similar to (2.7).

References

Bagheri, S., Schlatter, P., Schmid, P.J. & Henningson, D.S. 2009 Global stability of a jet in crossflow. *J. Fluid Mech.* **624**, 33–44.

Balasubramaniyan, M., Kushwaha, A., Guan, Y., Feng, J., Liu, P., Gupta, V. & Li, L.K. 2021 Global hydrodynamic instability and blowoff dynamics of a bluff-body stabilized lean-premixed flame. *Phys. Fluids* **33** (3), 34103.

Bilger, R. 2004 Some aspects of scalar dissipation. *Flow Turbul. Combust.* **72** (2–4), 93–114.

Brouzet, D., Haghiri, A., Talei, M., Brear, M.J., Schmidt, O.T., Rigas, G. & Colonius, T. 2020 Role of coherent structures in turbulent premixed flame acoustics. *AIAA J.* **58** (6), 2635–2642.

Brouzet, D., Krisna, B., McCormick, D., Reimann, C.A., Mendoza, J. & Ihme, M. 2024 Analysis of direct and indirect noise in a next-generation aviation gas turbine combustor. *Combust. Flame* **260**, 113249.

Bushell, K.W. 1971 A survey of low velocity and coaxial jet noise with application to prediction. *J. Sound Vib.* **17** (2), 271–282.

Chen, Z.X., Langella, I., Swaminathan, N., Stöhr, M., Meier, W. & Kolla, H. 2019*a* Large eddy simulation of a dual swirl gas turbine combustor: flame/flow structures and stabilisation under thermoacoustically stable and unstable conditions. *Combust. Flame* **203**, 279–300.

Chen, Z.X. & Swaminathan, N. 2020 Influence of fuel plenum on thermoacoustic oscillations inside a swirl combustor. *Fuel* **275**, 117868.

Chen, Z.X., Swaminathan, N., Stöhr, M. & Meier, W. 2019*b* Interaction between self-excited oscillations and fuel–air mixing in a dual swirl combustor. *Proc. Combust. Inst.* **37** (2), 2325–2333.

Clavin, P. & Siggia, E.D. 1991 Turbulent premixed flames and sound generation. *Combust. Sci. Technol.* **78** (1–3), 147–155.

Crighton, D.G., Dowling, A.P., Williams, J.E.F., Heckl, M. & Leppington, F.G. 1992 Thermoacoustic sources and instabilities. In *Modern Methods in Analytical Acoustics: Lecture Notes*, pp. 387–405. Springer.

Dowling, A.P. & Hubbard, S. 2000 Instability in lean premixed combustors. *Proc. Inst. Mech. Engng Part A: J. Power Energy* **214** (4), 317–332.

Dowling, A.P. & Mahmoudi, Y. 2015 Combustion noise. *Proc. Combust. Inst.* **35** (1), 65–100.

Dunstan, T.D., Minamoto, Y., Chakraborty, N. & Swaminathan, N. 2013 Scalar dissipation rate modelling for large eddy simulation of turbulent premixed flames. *Proc. Combust. Inst.* **34** (1), 1193–1201.

DUROX, D., SCHULLER, T., NOIRAY, N., BIRBAUD, A.L. & CANDEL, S. 2009 Rayleigh criterion and acoustic energy balance in unconfined self-sustained oscillating flames. *Combust. Flame* **156** (1), 106–119.

EHSANIDERAKHSHAN, F., MAZAHERI, K. & MAHMOUDI, Y. 2020 Large eddy simulation on combustion noise in a non-premixed turbulent free flame: effect of oxygen enhancement. *Energy* **210**, 118534.

EMERSON, B., O'CONNOR, J., JUNIPER, M. & LIEUWEN, T. 2012 Density ratio effects on reacting bluff-body flow field characteristics. *J. Fluid Mech.* **706**, 219–250.

FRIC, T.F. & ROSHKO, A. 1994 Vortical structure in the wake of a transverse jet. *J. Fluid Mech.* **279**, 1–47.

FROUD, D., O'DOHERTY, T. & SYRED, N. 1995 Phase averaging of the precessing vortex core in a swirl burner under piloted and premixed combustion conditions. *Combust. Flame* **100** (3), 407–412.

GUPTA, A., LILLEY, D. & SYRED, N. 1984 Swirl Flows.Abacus Press.

HIRSCH, C., WÄSLE, J., WINKLER, A. & SATTELMAYER, T. 2007 A spectral model for the sound pressure from turbulent premixed combustion. *Proc. Combust. Inst.* **31** (1), 1435–1441.

HUANG, Y. & YANG, V. 2009 Dynamics and stability of lean-premixed swirl-stabilized combustion. *Prog. Energy Combust. Sci.* **35** (4), 293–364.

IHME, M. 2017 Combustion and engine-core noise. *Annu. Rev. Fluid Mech.* **49** (1), 277–310.

IHME, M., BODONY, D. & PITSCH, H. 2006 Prediction of combustion-generated noise in non-premixed turbulent jet flames using LES. In *12th AIAA/CEAS Aeroacoustics Conf. (27th AIAA Aeroacoustics Conference)*. AIAA Paper 2006-2614. AIAA.

ILAK, M., SCHLATTER, P., BAGHERI, S. & HENNINGSON, D.S. 2012 Bifurcation and stability analysis of a jet in cross-flow: onset of global instability at a low velocity ratio. *J. Fluid Mech.* **696**, 94–121.

JOVANOVIĆ, M.R., SCHMID, P.J. & NICHOLS, J.W. 2014 Sparsity-promoting dynamic mode decomposition. *Phys. Fluids* **26** (2), 24103. arXiv: 1309.4165.

KARAGOZIAN, A.R. 2010 Transverse jets and their control. *Prog. Energy Combust. Sci.* **36** (5), 531–553.

KLEIN, S.A. & KOK, J.B. 1999 Sound generation by turbulent non-premixed flames. *Combust. Sci. Technol.* **149** (1), 267–295.

KNAUS, R. & PANTANO, C. 2009 On the effect of heat release in turbulence spectra of non-premixed reacting shear layers. *J. Fluid Mech.* **626**, 67–109.

KOLLA, H., HAWKES, E.R., KERSTEIN, A.R., SWAMINATHAN, N. & CHEN, J.H. 2014 On velocity and reactive scalar spectra in turbulent premixed flames. *J. Fluid Mech.* **754** (1), 456–487.

KOOPMAN, B.O. 1931 Hamiltonian systems and transformation in Hilbert Space. *Proc. Natl Acad. Sci.* **17** (5), 315–318.

KOTAKE, S. & TAKAMOTO, K. 1987 Combustion noise: effects of the shape and size of burner nozzle. *J. Sound Vib.* **112** (2), 345–354.

KOTAKE, S. & TAKAMOTO, K. 1990 Combustion noise: effects of the velocity turbulence of unburned mixture. *J. Sound Vib.* **139** (1), 9–20.

LANGELLA, I., SWAMINATHAN, N. & PITZ, R.W. 2016 Application of unstrained flamelet SGS closure for multi-regime premixed combustion. *Combust. Flame* **173**, 161–178.

LAPORTE, F. & CORJON, A. 2000 Direct numerical simulations of the elliptic instability of a vortex pair. *Phys. Fluids* **12** (5), 1016–1031.

LIEUWEN, T. 2001 Theory of high frequency acoustic wave scattering by turbulent flames. *Combust. Flame* **126** (1–2), 1489–1505.

LIEUWEN, T., MOHAN, S., RAJARAM, R. & Preetham 2006 Acoustic radiation from weakly wrinkled premixed flames. *Combust. Flame* **144** (1–2), 360–369.

LIEUWEN, T., RAJARAM, R., NEUMEIER, Y. & NAIR, S. 2002 Measurements of incoherent acoustic wave scattering from turbulent premixed flames. *Proc. Combust. Inst.* **29** (2), 1809–1815.

LIEUWEN, T.C. 2012 *Unsteady Combustor Physics*. Cambridge University Press.

LIGHTHILL, M. 1952 On sound generated aerodynamically. I. General theory. *Proc. R. Soc. London. Ser. A: Math. Phys. Sci.* **211**(1107), 564–587.

LIU, Y., DOWLING, A.P., SWAMINATHAN, N., MORVANT, R., MACQUISTEN, M.A. & CARACCIOLO, L.F. 2014 Prediction of combustion noise for an aeroengine combustor. *J. Propul. Power* **30** (1), 114–122.

LIU, Y. & ECHEKKI, T. 2015 Modelling of combustion noise spectrum using temporal correlations of heat release rate from turbulent premixed flames. In *21st AIAA/CEAS Aeroacoustics Conference*. AIAA Paper 2015-2970. AIAA.

LYRINTZIS, A.S. 2003 Surface integral methods in computational aeroacoustics – from the (CFD) near-field to the (acoustic) far-field. *Intl J. Aeroacoust.* **2** (2), 95–128.

MARBLE, F.E. & CANDEL, S.M. 1977 Acoustic disturbance from gas non-uniformities convected through a nozzle. *J. Sound Vib.* **55** (2), 225–243.

MASSEY, J.C., CHEN, Z.X., STÖHR, M., MEIER, W. & SWAMINATHAN, N. 2022 On the blow-off correlation for swirl-stabilised flames with a precessing vortex core. *Combust. Flame* **239**, 111741.

MASSEY, J.C., CHEN, Z.X. & SWAMINATHAN, N. 2019*a* Lean flame root dynamics in a gas turbine model combustor. *Combust. Sci. Technol.* **191** (5–6), 1019–1042.

MASSEY, J.C., LANGELLA, I. & SWAMINATHAN, N. 2019*b* A scaling law for the recirculation zone length behind a bluff body in reacting flows. *J. Fluid Mech.* **875**, 699–724.

MASSEY, J.C., TANAKA, Y. & SWAMINATHAN, N. 2023 Application of a two-progress variable model for carbon monoxide emissions from turbulent premixed and partially premixed enclosed flames. *Combust. Flame* **258**, 113047.

MEIER, W., DUAN, X.R. & WEIGAND, P. 2006 Investigations of swirl flames in a gas turbine model combustor: II. Turbulence–chemistry interactions. *Combust. Flame* **144** (1–2), 225–236.

MERK, M., GAUDRON, R., SILVA, C., GATTI, M., MIRAT, C., SCHULLER, T. & POLIFKE, W. 2019 Prediction of combustion noise of an enclosed flame by simultaneous identification of noise source and flame dynamics. *Proc. Combust. Inst.* **37** (4), 5263–5270.

MERK, M., POLIFKE, W., GAUDRON, R., GATTI, M., MIRAT, C. & SCHULLER, T. 2018 Measurement and simulation of combustion noise and dynamics of a confined swirl flame. *AIAA J.* **56** (5), 1930–1942.

MURUGAVEL, A.B., MASSEY, J.C., TANAKA, Y. & SWAMINATHAN, N. 2024 The effect of methane addition on reacting hydrogen jets in crossflow. *Intl J. Hydrogen Energy* **80**, 57–67.

NANDULA, S.P. 2003 Lean premixed flame structure in intense turbulence: Rayleigh/Raman/LIF measurements and modeling. *PhD thesis*, Vanderbilt University.

PAN, J.C., SCHMOLL, W.J. & BALLAL, D.R. 1990 Turbulent combustion properties behind a confined conical stabilizer. In Proc. ASME Turbo Expo, Vol. **3**. American Society of Mechanical Engineers (ASME).

PIERCE, C.D. & MOIN, P. 1998 A dynamic model for subgrid-scale variance and dissipation rate of a conserved scalar. *Phys. Fluids* **10** (12), 3041–3044.

RAJARAM, R. & LIEUWEN, T. 2009 Acoustic radiation from turbulent premixed flames. *J. Fluid Mech.* **637**, 357–385.

SCHMID, P.J. 2010 Dynamic mode decomposition of numerical and experimental data. *J. Fluid Mech.* **656**, 5–28.

SCHMID, P.J. 2022 Dynamic mode decomposition and its variants. *Annu. Rev. Fluid Mech.* **54** (1), 225–254.

SILVA, C.F., LEYKO, M., NICOUD, F. & MOREAU, S. 2013 Assessment of combustion noise in a premixed swirled combustor via large-eddy simulation. *Comput. Fluids* **78**, 1–9.

SILVA, C.F., MERK, M., KOMAREK, T. & POLIFKE, W. 2017 The contribution of intrinsic thermoacoustic feedback to combustion noise and resonances of a confined turbulent premixed flame. *Combust. Flame* **182**, 269–278.

SINGH, K.K., FRANKEL, S.H. & GORE, J.P. 2004 Study of spectral noise emissions from standard turbulent nonpremixed flames. *AIAA J.* **42** (5), 931–936.

SINGH, K.K., ZHANG, C., GORE, J.P., MONGEAU, L. & FRANKEL, S.H. 2005 An experimental study of partially premixed flame sound. *Proc. Combust. Inst.* **30** (2), 1707–1715.

STEINBERG, A.M., SADANANDAN, R., DEMB, C., KUTNE, P. & MEIER, W. 2013 Structure and stabilization of hydrogen jet flames in cross-flows. *Proc. Combust. Inst.* **34** (1), 1499–1507.

STRAHLE, W.C. 1973 A review of combustion generated noise. In *AIAA Aero-Acoustics Conference*. AIAA Paper, 73-1023. AIAA.

STRAHLE, W.C. 1978 Combustion noise. *Prog. Energy Combust. Sci.* **4** (3), 157–176.

SWAMINATHAN, N., BALACHANDRAN, R., XU, G. & DOWLING, A.P. 2011*a* On the correlation of heat release rate in turbulent premixed flames. *Proc. Combust. Inst.* **33** (1), 1533–1541.

SWAMINATHAN, N. & BRAY, K.N. 2005 Effect of dilatation on scalar dissipation in turbulent premixed flames. *Combust. Flame* **143** (4), 549–565.

SWAMINATHAN, N., XU, G., DOWLING, A.P. & BALACHANDRAN, R. 2011*b* Heat release rate correlation and combustion noise in premixed flames. *J. Fluid Mech.* **681**, 80–115.

TAM, C.K. 2015 The spectral shape of combustion noise. *Intl J. Aeroacoust.* **14** (3–4), 431–456.

TENNEKES, H. & LUMLEY, J. 1972 *A First Course in Turbulence*. MIT Press.

TU, J.H., ROWLEY, C.W., LUCHTENBURG, D.M., BRUNTON, S.L., KUTZ, J.N. 2014 On dynamic mode decomposition: theory and applications. *J. Comput. Dyn.* **1** (2), 391–421.

ULLRICH, W.C., MAHMOUDI, Y., LACKHOVE, K., FISCHER, A., HIRSCH, C., SATTELMAYER, T., DOWLING, A.P., SWAMINATHAN, N., SADIKI, A. & STAUFER, M. 2018 Prediction of combustion noise in a model combustor using a network model and a LNSE approach. *J. Engng Gas Turbines Power* **140** (4), 041501-1–041501-10.

WALEFFE, F. 1990 On the three-dimensional instability of strained vortices. *Phys. Fluids A* **2** (1), 76–80.

WÄSLE, J., WINKLER, A. & SATTELMAYER, T. 2005 Spatial coherence of the heat release fluctuations in turbulent jet and swirl flames. *Flow Turbul. Combust.* **75** (1–4), 29–50.

WÄSLE, J.G. 2007 Vorhersage der Lärmemission turbulenter Vormischflammen. *PhD thesis, Technical University of Munich, Germany.*

WEIGAND, P., MEIER, W., DUAN, X.R., STRICKER, W. & AIGNER, M. 2006 Investigations of swirl flames in a gas turbine model combustor: I. Flow field, structures, temperature, and species distributions. *Combust. Flame* **144** (1–2), 205–224.

WINKLER, A., WÄSLE, J. & SATTELMAYER, T. 2005 Experimental investigations on the acoustic efficiency of premixed swirl stabilized flames. In *Collect. Tech. Pap. – 11th AIAA/CEAS Aeroacoustics Conf.*, vol. **2**, pp. 1387–1405. AIAA.

ZHANG, F., ZIRWES, T., HABISREUTHER, P., BOCKHORN, H., TRIMIS, D., NAWROTH, H. & PASCHEREIT, C.O. 2019 Impact of combustion modeling on the spectral response of heat release in LES. *Combust. Sci. Technol.* **191** (9), 1520–1540.